Experimental study and kinetic modeling of high temperature and pressure CO$_2$ mineralization

Maximilian Berndsen [a,b,*], Selçuk Erol [c], Taylan Akın [d], Serhat Akın [e], Isabella Nardini [b], Adrian Immenhauser [a,b], Mathias Nehler [b]

[a] Institute of Geology, Mineralogy, and Geophysics, Ruhr-University Bochum, Universitätsstraße 150, Bochum 44801, Germany
[b] Fraunhofer IEG, Fraunhofer Research Institution for Energy Infrastructures and Geothermal Systems IEG, Am Hochschulcampus 1/IEG, Bochum 44801, Germany
[c] Department of Energy Systems Engineering, Engineering Faculty, Izmir Institute of Technology (IZTECH), Urla-Izmir 35430, Turkey
[d] Geothermal Application and Research Center, Pamukkale University, Denizli, Turkey
[e] Petroleum and Natural Gas Engineering Department, Middle East Technical University (METU), ODTÜ Üniversiteler Mah.Dumlupınar Blv.No:1, Çankaya Ankara 06800, Turkey

ABSTRACT

The potential for *in-situ* CO$_2$ sequestration was analyzed experimentally for one basaltic hyaloclastite sample from the Nesjavellir geothermal reservoir in Iceland and three metasedimentary rock samples from the Kızıldere geothermal field in Turkey. Based on batch reaction experiments, this paper demonstrates the interaction between a CO$_2$ gas-charged fluid and rock samples from these reservoirs. The experiments were conducted at 260 °C and 0.8 MPa, and 105 °C and 17 MPa for the basaltic and metasedimentary rocks, respectively. The experimental results indicate that CO$_2$ sequestration within the glassy basaltic rocks is hampered by zeolite, chlorite, and anhydrite, which compete with carbonate minerals to uptake divalent cations at the P-T conditions applied. In contrast, the carbonation process for the metasedimentary rocks is inhibited by their mineralogical composition. Generally, these rocks are less reactive and provide an insufficient supply of divalent cations. The batch reactor experiments were numerically simulated with the PHREEQC geochemical modeling program. The simulations indicate that CO$_2$ sequestration is feasible at the tested P-T conditions, provided that silicate and SO$_4$ mineralization is suppressed for the basaltic rocks and that there is an effective source of divalent cations for the metasedimentary rocks.

1. Introduction

Rising greenhouse gas concentrations, particularly CO$_2$, in the atmosphere and their impact on global climate have triggered significant research on emission mitigation and carbon capture methods (Gunnarsson et al., 2018; Matter et al., 2016; Metz et al., 2005 , among others). A particularly prominent study area is the carbonation of anthropogenically emitted CO$_2$, aiming to mitigate its impact on the natural short to mid-term carbon cycle (Oelkers et al., 2008; Raza et al., 2022; Snæbjörnsdóttir et al., 2020). The underlying concept is that CO$_2$ is removed from the atmosphere by reacting in aqueous solutions with divalent metal cations, such as Ca^{2+}, Mg^{2+}, and Fe^{2+}, to form carbonate minerals (Gislason et al., 2010; Metz et al., 2005; Oelkers et al., 2008; Oelkers and Schott, 2005; Snæbjörnsdóttir et al., 2018).

The CarbFix1 and CarbFix2 projects carried out in Iceland demonstrated that the co-produced CO$_2$ (g) from geothermal power plants could be recharged into the effluent fluid and stored through mineralization in basaltic rock formations, even at high enthalpy reservoirs (Aradóttir et al., 2012; Clark et al., 2020; Snæbjörnsdóttir et al., 2020). Snæbjörnsdóttir et al. (2018) assessed CO$_2$-fluid-rock interaction for the CarbFix1 injection site at Hellisheidi, southwest Iceland. Their reaction path model calculations were calibrated based on the measured fluid components at several observation wells. The study indicates that the appropriate pH for CO$_2$ mineralization in basaltic reservoirs is about 5.2 to 6.5 at temperatures between 20 and 50 °C. For the high-temperature CarbFix2 injection site at Hellisheidi, Ratouis et al. (2021) performed one-dimensional reactive transport simulations at temperatures above 220 °C. Their results indicate that silicates, such as epidote and

chamosite, take up aqueous Mg^{2+}, Ca^{2+}, or Fe^{2+} at high temperatures, limiting carbonate mineralization.

Galeczka et al. (2022) performed reaction path modeling to simulate fluid-rock interactions along the flow paths between the injection and production wells of the Nesjavellir geothermal reservoir. The calculations consider an increase in temperature from 84 to 300 °C while the fluid progresses from the injection well deeper into the reservoir. Based on their results, these authors estimate that 70 % of the injected CO_2 can be mineralized along the flow path. In this system, they found that carbonation becomes limited at temperatures higher than 165 °C because silicates such as epidote, clays, wollastonite, actinolite, and zeolites compete against carbonates for divalent cations.

The experiments and models presented in this study form part of the Geothermal Emission Control Project (GECO), which extends the techniques and gained experiences from CarbFix to other European geothermal systems in Iceland, Italy, Germany, and Turkey with different reservoir lithologies and temperatures (Sigfusson et al., 2021). We performed a series of rock-fluid-CO_2 batch reactor experiments that simulated the pressure and temperature conditions during fluid injection at two geothermal reservoirs and enabled monitoring of the fluid's chemical evolution. The experiments were conducted with a basaltic hyaloclastite rock sample from the Nesjavellir geothermal reservoir in Iceland at a temperature of 260 °C and three metasedimentary rock samples from the Kızıldere geothermal field in Turkey at a temperature of 105 °C. In addition, we simulated the experiments numerically with kinetic batch reaction models using the PHREEQC geochemical calculation program (Parkhurst and Appelo, 2013).

The CO_2 and H_2S injection into high-temperature reservoirs (>250 °C) at Hellisheidi (CarbFix2 site) and Nesjavellir was supported by geochemical well-monitoring and modeling (Clark et al., 2018; Clark et al., 2020; Galeczka et al., 2022; Gunnarsson et al., 2018; Ratouis et al., 2021; Ratouis et al., 2022), but laboratory experiments that investigate the geochemical reactions and CO_2 sequestration efficiency were not conducted for such high temperatures. Our 260 °C batch reaction experiment results, using reservoir rock and fluid samples from Nesjavellir, complement the existing analyses and models. Furthermore, by combining our experimental work with numerical modeling, we identified inconsistencies in the modeled mineral reactions that would go unnoticed without the experimental verification.

The CO_2 injection at the Kızıldere geothermal field has been previously investigated using reactive transport modeling (Erol et al., 2022, 2023), but the experimental data on rock-fluid-CO_2 interactions presented here have so far been lacking for the metasediments of the reservoir. Geochemical modeling of the batch reaction experiments revealed that the mineral kinetic rate data from the literature differ from those applicable to the metasedimentary rocks. By matching them to our experimental results, we derived new kinetic rate constants that more accurately describe the complex multiphase system.

With the experiments and simulations, we determined the mineral reactions expected for the tested lithologies at the respective P-T reservoir conditions and disclosed the potential and challenges for CO_2 sequestration. Furthermore, model capabilities and limitations are examined by matching the numerical simulations to the batch reaction experiments. The outcome of our work is relevant for the CO_2 storage projects at Nesjavellir and Kızıldere reservoirs but also has wider significance for *in-situ* CO_2 sequestration research in general.

2. Material and methods

Four selected rock samples, one drill core from Iceland and three specimens from Turkey, have been used to perform a series of CO_2-fluid-rock dissolution/precipitation reaction experiments in a heated and pressurized batch reactor. The Icelandic sample (IC-1) originates from a core drilled through basaltic hyaloclastite from well NJ-18 of the Nesjavellir geothermal field. The core is formed by partially palagonized glass shards with interstitial zeolites and a volumetrically subordinate

calcite phase. Phenocrysts in shards of sideromelane are dominated by plagioclase, but pyroxene and olivine are also present (Tables 1 and 2). The rock specimens from Turkey comprise Fe-oxide/sulfide-mica-carbonate-quartz schists (TU-1), Fe-oxide-mica-quartz schists (TU-2), and andalusite-mica-quartz schists (TU-3), with an increasing quartz content from samples 1 through 3 (Tables 1 and 2). The constituent minerals of these rocks are predominantly quartz, muscovite, chlorite, clay minerals such as montmorillonite and its endmembers, and rarely pyrite and hematite. Aluminosilicate (e.g., albite) and Ca/Mg carbonates (calcite and dolomite) can be secondary minerals. The samples were collected at outcrops near the village of Yenicekent that represent the lithologies of the reservoir section of the pilot injection well at the Kızıldere geothermal field (Fig. 1). The Kızıldere geothermal site in Turkey is one of the demonstration sites to test the application of the CarbFix method to metamorphic schist and marble host rocks.

The experimental fluids used in this study originate from the test sites in Iceland and Turkey. These are effluent reservoir water from well NJ-18 of the Nesjavellir geothermal field in Iceland, effluent reservoir water from the Kızıldere power plant in Turkey, and condensate water that is stored in a bypass pond for reinjection at the Kızıldere power plant.

2.1. Experimental setup

Batch reactor experiments were conducted in a stirred pressure vessel of 1.1 l volume designed for a maximum pressure of 35 MPa and a maximum temperature of 350 °C (Parr Instrument; 4626 series; Fig. 2). All wetted reactor parts and connections, including the syringe pumps, are made of corrosion-resistant Hastelloy C-276. The reactor has three ports for fluid injection, fluid sampling, and gas supply, and another three ports hold the manometer, the thermocouple, and a rupture disk. A nitrogen gas bottle with a pressure regulator is connected to adjust the pressure inside the vessel and purge the sampling line. The reactor fluid is sampled through a line running from the bottom of the reactor

Table 1

Rock sample composition based on thin section microscopy. Volume fractions were determined through point counting. Phase identification was assisted by EDX and XRD analysis. The volumetric significance was calculated for 75 g of sample material, corresponding to the sample mass used for the experiments.

Sample Mineralogy			
Sample	Constituents	Volume fraction in %	Volumetric significance (75 g rock sample) in mmol
IC-1	Sideromelane	24.2	143.8
	Palagonite	51.7	307.1
	Zeolite	12.4	13.7
	Clay	7.0	12.7
	Plagioclase	2.9	8.0
	Calcite	1.1	8.3
	Pyroxene	0.6	2.6
	Olivine	0.1	0.7
TU-1	Quartz	69.7	848.5
	Carbonate	25	108.4
	Muscovite	2.7	5.2
	Clay	1.6	3.1
	Fe-oxide/sulfide	0.7	4.5
	Epidote	0.3	5.7
TU-2	Quartz	58.4	700.8
	mica	25.1	47.8
	Clay	14.1	27.1
	Fe-oxide/sulfide	2.0	17.7
	andalusite	0.4	2.1
TU-3	Quartz	94.1	1167.4
	Muscovite	2.5	4.9
	Paragonite	1.3	2.6
	Andalusite	1.9	10.3
	Fe-oxide/sulfide	0.2	1.8

Table 2

Glass and mineral compositions measured by XRD and EDX using fresh sample material prior to the experiments. Note that only elements heavier than carbon could be detected by EDX analysis. The accuracy of some EDX analyses was limited due to interferences between mineral phases, resulting in mixed signals. The EDX measurement classified as either pyroxene or olivine could not be assigned with certainty.

Glass and mineral compositions			
Sample	Mineral / Glass	XRD	EDX
IC-1	Basaltic glass	–	$Si_{1.00}O_{3.16}Ca_{0.13}Al_{0.32}Fe_{0.31}Mg_{0.09}Na_{0.07}K_{0.1}Ti_{0.06}$
	Zeolite	$NaAlSi_2O_6 \cdot 3H_2O$	$Ca_{0.09}Al_{0.56}Na_{0.14}Si_{1.00}O_{3.00}$
	Kaolinite	$Al_2(Si_2O_8)(OH)_4$	–
	Montmorillonite	$(Na, Ca)_{0.3}Al_2(Si, Al)_4O_{10}(OH)_2 \cdot n\,H_2O$	–
	Anorthite	$Ca(Al_2Si_2O_8)$	–
	Plagioclase	$(Na_{0.75}Ca_{0.25})(Al_{1.26}Si_{2.74}O_8)$	–
	Calcite	$CaCO_3$	$Ca_{0.34}O_{1.00}$
	Pyroxene/Olivine	–	$Mg_{0.73}Fe_{0.43}Al_{0.06}Si_{1.00}O_{3.26}$
TU-1	Quartz	SiO_2	$Si_{1.00}O_{1.00}$
	Dolomite	$Ca(Mg_{0.67}Fe_{0.33})(CO_3)_2$	$Ca_{1.00}Fe_{0.80}Mg_{0.68}O_{4.77}$
	Muscovite	$K_{0.92}Na_{0.08}Al_{1.78}Fe_{0.22}(Al_{0.82}\ldots\ldots Si_{3.18}O_{10})(OH)_{1.85}O_{0.08}F_{0.07}$	$K_{0.27}Al_{0.76}Si_{1.00}O_{1.94}Fe_{0.04}Ti_{0.04}Mg_{0.02}Ca_{0.01}Na_{0.01}$
	Illite	$KAl_2Si_3AlO_{10}(OH)_2$	–
	Kaolinite	$Al_2(Si_2O_8)(OH)_4$	–
	Gypsum	$CaSO_4 \cdot 2H_2O$	–
	Fe-oxide	–	$Fe_{1.00}O_{0.78}Si_{0.09}Al_{0.01}$
	Pyrite	–	$Fe_{1.00}S_{1.44}O_{0.15}$
	Epidote	–	–
TU-2	Quartz	SiO_2	$Si_{1.00}O_{1.36}$
	Muscovite	$K_{0.92}Na_{0.08}Al_{1.78}Fe_{0.22}(Al_{0.82}\ldots\ldots Si_{3.18}O_{10})(OH)_{1.85}O_{0.08}F_{0.07}$	$K_{0.23}Al_{0.80}Si_{1.00}O_{1.95}Na_{0.04}$
	Paragonite		$Na_{0.17}K_{0.05}Al_{0.88}Si_{1.00}O_{1.80}Ca_{0.01}$
	Montmorillonite	$(Na, Ca)_{0.3}Al_2(Si, Al)_4O_{10}(OH)_2 \cdot n\,H_2O$	–
	Andalusite	–	–
	Fe-oxide	–	$Fe_{1.00}O_{1.07}Si_{0.07}Al_{0.03}$
	Pyrite	–	–
	Rutile	TiO_2	$Ti_{1.00}O_{1.34}Si_{0.13}Al_{0.11}Na_{0.03}Fe_{0.02}$
TU-3	Quartz	SiO_2	$Si_{1.00}O_{0.76}Na_{0.02}$
	Muscovite	–	–
	Paragonite	–	$Na_{0.10}K_{0.02}Al_{0.55}Si_{1.00}O_{1.50}Fe_{0.02}Ca_{0.01}$
	Andalusite	–	$Al_{1.50}Si_{1.00}O_{1.27}$
	Fe-Ti-oxide	–	$Fe_{1.00}Ti_{0.32}O_{1.03}Si_{0.14}Al_{0.01}$
	Pyrite	–	–

through a pressure valve to an outlet. A Teledyne ISCO 500D syringe pump with a capacity of 507 ml was used to inject fluids enriched in CO_2 at corresponding pressures to the bottom of the reactor (Fig. 2).

2.2. Experimental protocol

The reactor was filled with 750 ml of effluent reservoir water and 75 g of rock powder from the corresponding location for each experiment. Apart from a small rock chip that functioned as a precipitation substratum to detect mineral precipitations, the rock samples were crushed to grain sizes smaller than 125 µm. To prevent the fine sample powder from clogging the vessel's bottom, it was confined to a fine-meshed stainless-steel wire basket hanging in the vessel. This allowed a magnetic stir bar to keep the fluid slowly agitated. After filling and sealing the vessel, the system was purged with nitrogen to remove air in the headspace and O_2 from the liquid. The temperature was then increased to the desired target values of 260 °C for the basaltic sample (IC-1) and 105 °C for the metasedimentary samples (TU-1/-2/-3).

The temperature of 260 °C in the case of experiment IC-1 corresponds to the maximum measured temperature in the injection well NJ-18 before the start of fluid injection in 2018 (Galeczka et al., 2022; Snæbjörnsdóttir et al., 2020a). The temperature is expected to increase to about 300 °C in the reservoir with increasing distance to the injection well (Franzson, 2000; Galeczka et al., 2022).

The reservoir temperature of the Kızıldere geothermal field is typically 200–220 °C (Erol et al., 2022). The 105 °C fluid temperature applied to the metasedimentary sample experiments corresponds to the fluid injection temperature at the Kızıldere test site, representing the minimum temperature close to the injection well, where the volumetrically most important chemical reactions take place (Erol et al., 2022).

The pressure conditions inside the reactor were set through the

connection with a nitrogen gas supply. For the basaltic sample (IC-1), we aimed for the reported pressure at the bottom of well NJ-18, which reached about 20 MPa (Gunnarsdóttir et al., 2021). However, at that time, our laboratory setup did not meet the necessary safety requirements to deal with such high pressures, and the experiment was run with a lower pressure of 8 MPa. It seems plausible that the lower pressure did not significantly influence the experimental outcome as the effect of pressure on mineral-fluid reactions is usually less important than the effect of temperature (Langmuir, 1997).

Later, we adjusted the experimental setup and eliminated the safety concerns for the subsequent experiments TU-1/-2/-3, allowing higher pressure. The pressure for experiments TU-1/-2/-3 was set to 3.3 MPa, corresponding to the fluid injection pressure at the pilot injection well. After CO_2 injection, the pressure was increased to the expected downhole pressure of 17 MPa at reservoir depth. Fluids were regularly sampled from the reactor, starting the day after the initial filling. Each experiment lasted 30 days, during which ten fluid samples of approximately 20 ml were taken. Thus, the rock-fluid ratio was altered with every fluid extraction.

A CO_2-enriched fluid was injected into the reactor under *in-situ* conditions after 5–6 days of fluid-rock equilibration time. For experiment IC-1, this fluid was distilled water in equilibrium with 99 % pure CO_2 at 0.75 MPa and 25 °C. For experiments TU-1/-2/-3, bypass brine-pond condensate water was used to equilibrate with 99 % pure CO_2 at 1.4 MPa and 25 °C. The set CO_2 partial pressures correspond to the injection fluids at the respective power plants. Equilibration was attained inside the syringe pumps that were used for injection. Pump A was filled with 300 ml of the respective liquid and about 200 ml of CO_2 at the corresponding pressure. Liquid and gas were left to equilibrate for at least 24 hours. Before injection, the gas phase was displaced by pumping approximately 250 ml of volume from pump A to pump B at constant
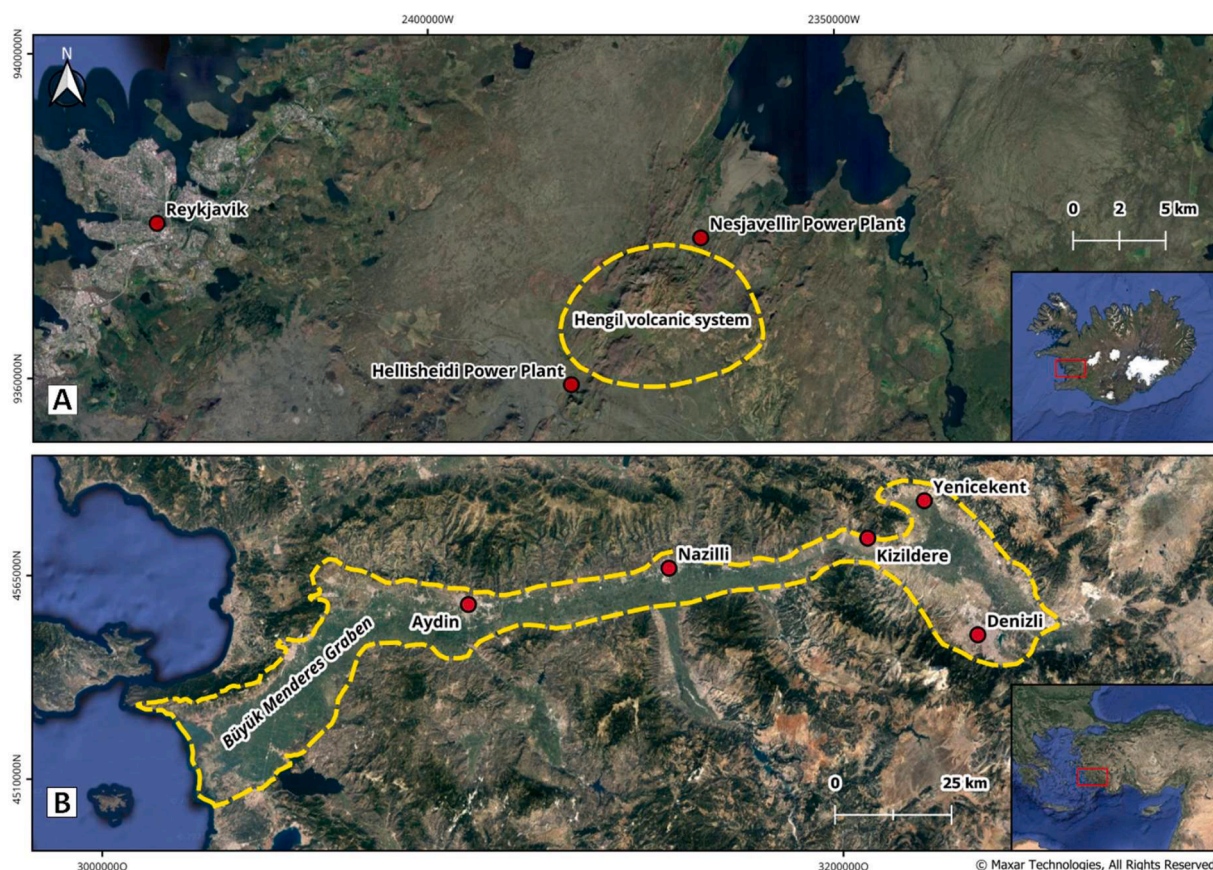
Fig. 1. Overview map showing the locations of the Nesjavellir (A) and Kızıldere (B) geothermal fields. (A) indicates the locations of the Nesjavellir and Hellisheidi geothermal power plants in Iceland that use heat from the Hengill volcanic system (roughly outlined with the yellow dotted line). (B) shows the location of the Kızıldere (power plant) and Yenicekent (sampling location) villages together with the towns of Aydin, Nazili, and Denizli in Turkey. They are located in the Büyük Menderes Graben structure, which hosts several geothermal fields (roughly outlined with the yellow dotted line).

Table 3

Fluid sample composition based on IC and ICP-OES measurements. CO_2 and HCO_3^- were determined by titration. Vellankatla spring water data are from Gysi and Stefánsson (2012a), and freshwater data are from Marieni et al. (2021a). The freshwater and Vellankatla spring-water data are referred to in the test.

Composition of fluid samples						
	Unit	NJ-18 Effluent Iceland	KZD-3 EPS Turkey	KZD-3 Bypass pond Turkey	Vellankatla Spring water	Freshwater
pH	–	7.90	9.77	8.78		8.99
T	°C	17.8	18.6	18.6		25
O_2	mg/l	9.30	8.93	8.58		
CO_2	mmol/l	0.025	–	–		
HCO_3^-	mmol/l	0.450	45.350	28.550		
Si	mg/l	230.330	271.988	166.104	7.2	236.6
Na	mg/l	97.189	1573.131	1184.199	6.2	146.28
K	mg/l	19.563	237.079	178.540	0.5	24.96
Mg	mg/l	0.001	0.017	1.019	0.923	
Ca	mg/l	0.211	3.248	6.652	2.8	0.4
Fe	mg/l	0.361	0.075	0.192	0.009	
Mn	mg/l	0.019	0.004	0.006		
Ba	mg/l	0.000	0.080	0.129		
Al	mg/l	1.115	0.547	0.476	0.03	1.35
B	mg/l	1.207	28.014	22.794		
Cl	mg/l	98.051	166.879	353.225	4.3	127.09
SO_4	mg/l	46.001	990.708	882.264	1.4	23.04
NO_3	mg/l	0.051	–	56.779		
F	mg/l	0.691	28.690	21.818		
Br	mg/l	0.470	1.326	–		

pressure. Afterward, the pressure in pump A was raised to match the pressure of the reactor vessel, and the accurate volume, defined by the target ratio between reactor fluid and injection fluid, was injected. The ratios amount to 10:1 for experiment IC-1 and 11:1 for experiments TU-1/-2/-3. These ratios correspond to the mixing ratios at the respective injection sites. Before the injection of the CO_2-enriched fluid, three fluid samples were already extracted from the reactor, which decreased the initial liquid volume by 60 ml. This volume reduction was considered to calculate the correct volume of the injection fluid to obtain the correct ratio. The resulting concentrations of dissolved CO_2 inside the reactor
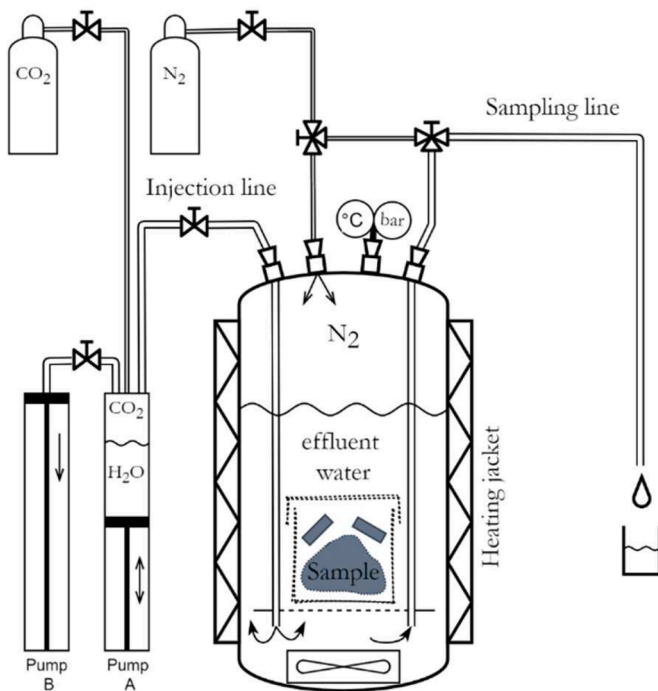
Fig. 2. Sketch of the experimental setup. H_2O inside pump A represents distilled water in the case of experiment IC-1. For the experiments TU-1, TU-2, and TU-3, pump A was filled with "KZD-3-Bypass brine-pond" condensate water. The water inside the reactor is effluent water from well NJ-18 in the case of experiment IC-1 and "KZD-3-EPS" water in the case of experiments TU-1, TU-2, and TU-3. Turn to Table 3 for the chemical fluid compositions.

were calculated to be 22.5 mmol/l for experiment IC-1 and 44.1 mmol/l for experiments TU-1/-2/-3. Shortly after injection, the reactor pressure of experiments TU-1/-2/-3 was adjusted towards the target value of 17 MPa, while the pressure for experiment IC-1 remained at 8 MPa.

2.3. Analytical

Fluid samples were analyzed at the Fraunhofer Research Institution for Energy Infrastructures and Geothermal Systems (IEG; Bochum) using inductively coupled plasma optical emission spectrometry (ICP-OES; Perkin Elmer Optima 8300) and ion chromatography (IC; Metrohm Eco IC with a Metrosep A Supp 17–150/4.0 column) to measure the cation and anion concentrations in the solutions, respectively.

Rock samples were analyzed before and after the batch reactor experiments through X-ray diffraction (XRD), gas sorption analysis applying the Brunauer-Emmett-Teller method (BET; Brunauer et al., 1938) and scanning electron microscopy (SEM) in combination with energy dispersive x-ray analysis (EDX) (Table 2). XRD and BET analyses were performed at the X-ray diffraction and fluorescence service of the petrology and mineralogy platform of the GET laboratory at the Centre National de la Recherche Scientifique (CNRS) in Toulouse, France, using a Bruker D2 Phaser diffractometer. SEM and EDX analyses were performed in the central laboratories of the Department for Geology, Mineralogy, and Geophysics of the Ruhr University Bochum on a ZEISS-Gemini2-Merlin high-resolution thermally aided field emission SEM. Prior to analysis, the SEM samples were gold-coated to create a conductive sample surface. Images were obtained at an acceleration voltage of 5 kV while the working distance and electron current were adjusted according to the sample's characteristics. A working distance of about 10 mm and an electron current of 100–200 pA was applied. For EDX analysis, the Oxford Instruments AZtecEnergy X-ray microanalysis software was used.

2.4. Modelling

In this study, the PHREEQC 3.7.3 geochemical modeling program (Parkhurst and Appelo, 2013) combined with the carbfix.dat (Voigt et al., 2018) and the llnl.dat (Parkhurst and Appelo, 2013; Wolery and Daveler, 1992) databases were applied to simulate the batch reactor experiments numerically. The carbfix.dat database was used to simulate the experiment with the basaltic rock as this database was created as an extension and improvement of the core10.dat database to model basalt-hosted fluid-rock interactions. Thermodynamic databases compiled for metamorphic rocks are currently limited. We used the llnl. dat database, which delineates pertinent endmembers of minerals occurring within the given system. In general, the selection of thermodynamic datasets is an *ad hoc* process, and the results will be more or less accurate depending on the similarity between the phases in the database and the phases involved in the experiments in terms of compositional variability and/or degree of crystallinity (Blasco et al., 2017).

We found that kinetic rate constants from the literature do not adequately reproduce the experimental results of the metasedimentary rocks. Therefore, we derived new kinetic rate constants that accurately describe our particular rock-fluid system by fitting them to our experimental results (Table 5).

For basaltic glass, we adopted the experimentally determined far-from-equilibrium surface area normalized basaltic glass dissolution rate equation of Gislason and Oelkers (2003). Heřmanská et al. (2022) regressed published basaltic glass dissolution rate data and updated the equation to the following:

$$r_+ = 1.08 \times 10^{-4} \; mol \; m^{-2} s^{-1} \; \times \; \exp\left(\frac{-21500 \; J \; mol^{-1}}{R \; T}\right)\left(\frac{a_{H^+}^3}{a_{Al^{3+}}}\right)^{\frac{1}{3}} \qquad (1)$$

where r_+ denotes the forward (or far-from-equilibrium) surface area normalized dissolution rate, R stands for the gas constant (8.314 J K^{-1} mol^{-1}), T signifies the temperature in K and a_{H^+} and $a_{Al^{3+}}$ represent the activity of the subscripted species.

Besides the kinetic parameters, the reactive surface area had to be defined for each mineral phase in the simulations. Surface area measurements were only available for the whole rock samples but not for single mineral phases. The surface areas have, therefore, been calculated assuming uniform spherical grains with a diameter of 100 μm given that 125 μm was the upper grain size limit for powder preparation. The calculated values were adapted for some minerals by considering their specific properties, e.g., higher surface areas for micas and clays. Surface area adjustment was also used to reach a good match with the experimental results. For basaltic glass, the measured BET surface area of the whole basalt sample was used, as basaltic glass is the sample's main phase, producing the most accurate results (Table 4).

Secondary minerals are selected based on the experimental results and data from previous studies (Erol et al., 2022; Galeczka et al., 2022; Marieni et al., 2021a). The simulations were performed in four steps, as explained in Fig. 3.

3. Results

3.1. Secondary mineralogy

The rock chips and rock powder placed inside the reactor were analyzed for secondary mineral precipitations by SEM. The rock powder was analyzed through XRD to detect changes in mineralogy not visible under the SEM.

3.1.1. Basaltic rock

Following the reactor experiment with the basaltic sample, the formerly barren sample surface was covered by a layer of secondary minerals consisting of zeolite, chlorite, clay, and anhydrite (Fig. 4, Table 6). Zeolites were mainly identified as analcime-wairakite solid
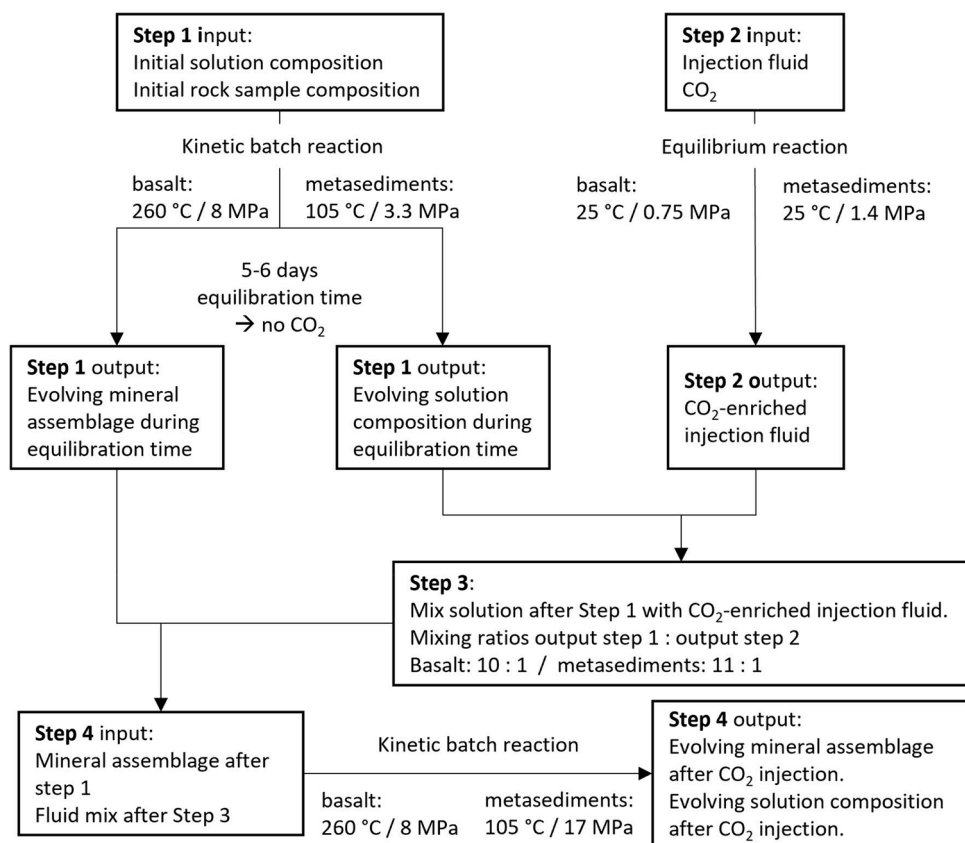
```
┌─────────────────────────────┐          ┌─────────────────────────────┐
│ Step 1 input:               │          │ Step 2 input:               │
│ Initial solution composition│          │ Injection fluid             │
│ Initial rock sample         │          │ CO₂                         │
│ composition                 │          │                             │
└─────────────────────────────┘          └─────────────────────────────┘
        Kinetic batch reaction                   Equilibrium reaction

   basalt:     │ metasediments:         basalt:        │ metasediments:
   260 °C / 8 MPa│ 105 °C / 3.3 MPa      25 °C / 0.75 MPa│ 25 °C / 1.4 MPa

           5-6 days
        equilibration time
          → no CO₂
```

```
┌──────────────────┐  ┌──────────────────┐  ┌──────────────────┐
│ Step 1 output:   │  │ Step 1 output:   │  │ Step 2 output:   │
│ Evolving mineral │  │ Evolving solution│  │ CO₂-enriched     │
│ assemblage during│  │ composition      │  │ injection fluid  │
│ equilibration    │  │ during           │  │                  │
│ time             │  │ equilibration    │  │                  │
│                  │  │ time             │  │                  │
└──────────────────┘  └──────────────────┘  └──────────────────┘
```

```
┌────────────────────────────────────────────────────────────────┐
│ Step 3:                                                          │
│ Mix solution after Step 1 with CO₂-enriched injection fluid.     │
│ Mixing ratios output step 1 : output step 2                      │
│ Basalt: 10 : 1  /  metasediments: 11 : 1                         │
└────────────────────────────────────────────────────────────────┘
```

```
┌──────────────────────────┐                  ┌──────────────────────────┐
│ Step 4 input:            │ Kinetic batch    │ Step 4 output:           │
│ Mineral assemblage after │   reaction       │ Evolving mineral         │
│ step 1                   │                  │ assemblage after CO₂     │
│ Fluid mix after Step 3   │ basalt: │ metased│ injection.               │
│                          │ 260 °C/ │ 105 °C/ │ Evolving solution        │
│                          │ 8 MPa   │ 17 MPa  │ composition after CO₂    │
│                          │         │         │ injection.               │
└──────────────────────────┘                  └──────────────────────────┘
```

Fig. 3. Schematic summary of the PHREEQC modeling steps.

solutions. Furthermore, scaling of minerals belonging to the clinoptilolite and analcime groups was found at the reactor wall. XRD analysis of the altered sample powder confirmed the precipitation of chlorite (chamosite) and a wairakite-type zeolite containing Na. Additionally, pyroxenes (diopside, ferrosilite and aerinite) were detected. Based on SEM and EDX analysis, pyroxenes were not encountered among the secondary minerals, and it remains unclear whether they represent primary or secondary minerals. Anhydrite was detected by XRD, but the low signal strength indicates that this mineral is an accessory phase.

In contrast, the SEM images show large anhydrite crystals on the altered sample surface. A comparison of the XRD results taken before with such obtained after the experiment reveals that the secondary minerals have formed at the expense of Na-chabazite, plagioclase, and clay minerals such as kaolinite and vermiculite. Calcite was detected in the assemblage before and after the experiment with no significant changes based on XRD and SEM. Basaltic glass is considered the main dissolving phase but cannot be detected by XRD.

3.1.2. Metasedimentary rocks

Experiment TU-1 formed small aggregates of Fe-rich smectite precipitated near pyrite and Fe-oxide minerals (Fig. 5). Analysis of these aggregates suggested that they consist of nontronite (

Table 6). No other precipitates were detected on the sample, whereas Si-oxide precipitated on the reactor walls. Experiments TU-2 and TU-3 did not produce any discernible precipitates on the sample surfaces, but there was scaling on the reactor wall, too. In the case of experiment TU-2, the scaling consisted of Na-oxide, Na-sulfate, and Na-fluorosulfate (kogarkoite). The scaling from experiment TU-3 was found to be Si-oxide.

3.2. Fluid chemistry

3.2.1. Basaltic rock

Most element concentrations initially increased in the solution after mixing rock powder and effluent water inside the reactor (Fig. 6). Before CO_2 injection, the solution had time to equilibrate, and elemental concentrations declined, as did the pH, both indicating mineral precipitation. In response to the CO_2 injection, the pH dropped below 6.5, and most element concentrations increased in the solution. While Na and Al continuously increased with the pH, the Si concentration decreased to its pre-injection level. Ca, Mg, and Fe concentrations show limited variation throughout the experiment.

3.2.2. Metasedimentary rocks

Besides the Ca and Mg concentrations of TU-1, the chemical fluid evolution of the three experiments followed similar trends. Silicon and Na concentrations declined but displayed a punctuated increase in response to the CO_2 injection. Silicon leveled off towards the end of the experiment, while Na showed a more arbitrary pattern. Aluminum concentrations reflected minor variability but generally decreased. Calcium and Mg concentrations of experiments TU-2 and TU-3 displayed limited variability throughout the experiment. In the context of experiment TU-1, however, Ca and Mg did show a distinct increase after CO_2 injection. Iron concentrations exhibited limited variations smaller than the sample's analytical error range. The pH of experiment TU-1 declined from 9.8 to 8.5 and was lowered by the injection of CO_2 toward a value of 7.4. No significant decrease in pH was measured before CO_2 injection for experiments TU-2 and TU-3. After injection, the pH was lowered to a value of around 7.9. However, as the pH was measured after the fluid was extracted from the reactor and depressurized, the pH inside the reactor might have been lower.

Table 4

Summary of parameters describing the kinetic mineral reaction rates used for modeling experiment IC-1. Notation: A_i: temperature-independent pre-exponential factor; E_{ai}: Activation energy; n_i: Reaction order.

IC-1	Surface area	Acidic mechanism			Neutral mechanism		Basic mechanism		
	$m^2 g^{-1}$	A_a $mol\ m^{-2}\ s^{-1}$	E_{aa} $J\ mol^{-1}$	n_a	A_b $mol\ m^{-2}\ s^{-1}$	E_{ab} $J\ mol^{-1}$	A_c $mol\ m^{-2}\ s^{-1}$	E_{ac} $J\ mol^{-1}$	n_c
Primary phases:									
Basaltic glass	30	See Section 2.4							
Chabazite-Na[1]	0.1	2.00×10^{-8}	58,000	0.7	1.59×10^{-12}	58,000	5.50×10^{-15}	58,000	-0.3
Kaolinite[2]	0.1	4.90×10^{-12}	22,200	0.777	6.61×10^{-14}	22,200	8.91×10^{-18}	17,900	0.472
Anorthite[3]	0.001	9.82×10^{4}	58,000	1.22	1.50×10^{-1}	60,000	1.50×10^{-5}	50,000	-0.35
Albite[3]	0.001	0.7	58,000	0.3	2.05×10^{-1}	60,000	1.50×10^{-5}	50,000	-0.35
Calcite[3]	0.01	3.27×10^{2}	16,000	1	4.73×10^{2}	35,000	1.64	35,000	1
Diopside[3]	0.001	8.55×10^{-5}	32,654	0.25	4.30×10^{-4}	43,866	–	–	–
Forsterite[3]	0.001	1.48×10^{5}	70,400	0.44	–	–	220	60,900	0.22
Potential alteration phases:									
Hematite[4]	0.01	2.57×10^{-9}	66,200	1	2.52×10^{-15}	66,200	–	–	–
Geothite[2]	0.01	–	–	–	1.64×10^{7}	86,500	–	–	–
Clinochlore-14A[2]	0.01	7.76×10^{-13}	88,000	0.5	3.02×10^{-13}	88,000	–	–	–
Chamosite	0.01	The rate of clinochlore-14A was used.							
Ferroactinolite[3]	0.001	3.00×10^{-3}	50,000	0.2	50,000	0.22	2.00×10^{-5}	48,000	–
Quartz[3]	0.01	4.03×10^{-14}	45,600	0.309	–	–	0.105	80,000	-0.41
Epidote[5]	0.001	1.14×10^{1}	60,000	0.56	5.13×10^{-5}	43,200	1.4×10^{-9}	42,300	-0.4
Siderite[4]	0.01	3.04×10^{-6}	61,000	0.75	2.23×10^{-9}	45,000	–	–	–
Magnesite[4]	0.01	2.50×10^{-5}	44,000	1	4.57×10^{-10}	34,000	–	–	–
Ankerite	0.01	The rate of siderite was used.							
Dolomite[4]	0.01	2.60×10^{-3}	36,100	0.75	2.20×10^{-8}	52,200	–	–	–
Dawsonite[4]	0.01	3.31×10^{-5}	49,400	0.982	1.29×10^{-7}	63,800	–	–	–
Anhydrite[2]	0.01	–	–	–	2.05×10^{-1}	14,299	–	–	–
Pyrite[2]	0.01	3.02×10^{-8}	50,800	-0.5	2.00×10^{-10}	50,800	2.82×10^{-5}	56,900	-0.5
Saponite-Fe-Fe[6]	1	1.05×10^{-13}	23,600	0.34	1.66×10^{-13}	35,000	3.02×10^{-17}	58,900	-0.4
Saponite-Fe-K[6]	1	1.05×10^{-13}	23,600	0.34	1.66×10^{-13}	35,000	3.02×10^{-17}	58,900	-0.4
Saponite-Mg-Mg[6]	1	1.05×10^{-13}	23,600	0.34	1.66×10^{-13}	35,000	3.02×10^{-17}	58,900	-0.4
Saponite-Mg-K[6]	1	1.05×10^{-13}	23,600	0.34	1.66×10^{-13}	35,000	3.02×10^{-17}	58,900	-0.4
Saponite-Mg-Fe[6]	1	1.05×10^{-13}	23,600	0.34	1.66×10^{-13}	35,000	3.02×10^{-17}	58,900	-0.4
Montmor-K[7]	1	1.95×10^{-13}	48,000	0.22	3.89×10^{-15}	48,000	3.90×10^{-12}	78,000	-0.13
Montmor-Mg[7]	1	1.95×10^{-13}	48,000	0.22	3.89×10^{-15}	48,000	3.90×10^{-12}	78,000	-0.13
Montmor-Na[7]	1	1.95×10^{-13}	48,000	0.22	3.89×10^{-15}	48,000	3.90×10^{-12}	78,000	-0.13
Analcime[1]	0.1	2.00×10^{-8}	58,000	0.7	1.59×10^{-12}	58,000	5.50×10^{-15}	58,000	-0.3
Laumontite[1]	0.1	2.00×10^{-8}	58,000	0.7	1.59×10^{-12}	58,000	5.50×10^{-15}	58,000	-0.3
Mordenite-Ca[1]	0.1	2.00×10^{-8}	58,000	0.7	1.59×10^{-12}	58,000	5.50×10^{-15}	58,000	-0.3
Stilbite-Ca[1]	0.1	2.00×10^{-8}	58,000	0.7	1.59×10^{-12}	58,000	5.50×10^{-15}	58,000	-0.3
Thomsonite[1]	0.1	2.00×10^{-8}	58,000	0.7	1.59×10^{-12}	58,000	5.50×10^{-15}	58,000	-0.3
Wairakite[1]	0.1	2.00×10^{-8}	58,000	0.7	1.59×10^{-12}	58,000	5.50×10^{-15}	58,000	-0.3

[1] For all zeolites, the rate law parameters of heulandite were used (Ratouis et al., 2021).
[2] From (Palandri and Kharaka, 2004)
[3] From Carbfix_kin.dat database (Heřmanská et al., 2022)
[4] From (Heřmanská et al., 2020)
[5] From (Marieni et al., 2021b)
[6] Based on smectite (K0.04Ca0.5(Al2.8Fe0.53Mg0.7)(Si7.65Al0.35)O20(OH)4) from (Palandri and Kharaka, 2004)
[7] Based on Montmorillonite (K0.318(Si3.975Al0.025)(Al1.509Fe0.205Mg0.283)(OH)2) from (Palandri and Kharaka, 2004)

4. Discussion

4.1. Reactor wall scaling

Precipitates formed on the reactor wall were most likely decoupled from fluid-rock equilibrium reactions. Evidence for this is that precipitates only formed at the interface between the reactor's liquid and gas phase, where they traced the fluctuating water level. In the authors' view, these precipitates did not form in equilibrium with the solution but represented evaporation precipitates along the water level. The mineral kogarkoite, for example, that was found in experiment TU-2, is known to form as a sublimate from the steam at hot springs (Pabst and Sharp, 1973; Žáček et al., 2015). The model calculations do not consider scaling formation at the reactor water line, but this process must be considered when comparing the modeled fluid evolution with the experimental outcome.

4.1.1. Kinetic model limitations

Kinetic mineral reaction modeling has many uncertainties, particularly when applied to complex multiphase systems. Aside from a comprehensive and consistent thermodynamic database, the accuracy of these kinetic calculations relies on the experimentally determined dissolution rate data. While these rate data may accurately describe the temporal evolution of dissolution reactions, their usage for modeling precipitation processes has yielded inconsistencies compared to natural and laboratory observations (Schott et al., 2009). Therefore, precipitation likely works on different mechanisms insufficiently described by dissolution rate equations (Heřmanská et al., 2022).

The experiments to determine dissolution rates are usually conducted using a pure phase mineral with a well-controlled pH buffer solution, ideally covering a wide range of temperature, pressure, and pH conditions. However, applying these rate constants to complex natural systems with multiple nonideal mineral phases and enriched fluids is impossible without limitations. To extend the significance of this work to more complex systems, the dissolution rates would need to be adapted with additional data. This work must take into account and quantify (i) the decrease in reaction rates and chemical affinity when approaching equilibrium, (ii) the catalytic or inhibiting effect of dissolved components that are not present in the mineral structure, (iii) the effect of varying mineral compositions in solid solution series, and (iv) the effect

Table 5

Summary of parameters describing the kinetic reaction rates for minerals used in models TU-1, TU-2, and TU-3. The models used the calculated rate constants in the first column, as the literature rate data did not produce adequate results. Published kinetic rate data are shown for comparison.

Notation: A_i: temperature-independent pre-exponential factor; E_{ai}: Activation energy; n_i: Reaction order.

	Calc. best-fit rate constants	Surface area	Acid mechanism			Neutral mechanism		Basic mechanism		
			A_a	E_{aa}	n_a	A_b	E_{ab}	A_c	E_{ac}	n_c
TU-1	mol m^{-2} s^{-1}	m^2 g^{-1}	mol m^{-2} s^{-1}	J mol^{-1}		mol m^{-2} s^{-1}	J mol^{-1}	mol m^{-2} s^{-1}	J mol^{-1}	
Quartz[3]	2.00×10^{-14}	0.022	4.03×10^{-4}	45,600	0.309	–	–	0.105	80,000	-0.41
Dolomite[4]	2.51×10^{-9}	0.021	2.60×10^{-3}	36,100	0.75	2.20×10^{-8}	52,200	–	–	–
Muscovite[3]	9.40×10^{-7}	0.015	1.26×10^{-4}	41,311	0.37	6.31×10^{-6}	39,301	3.16×10^{-5}	56,950	-0.22
Illite[8]	6.61×10^{-9}	0.443	1.00×10^{-2}	58,000	0.55	2.00×10^{-5}	54,000	1.49×10^{-3}	77,000	0.35
Kaolinite[2]	5.11×10^{-7}	0.110	4.90×10^{-12}	22,200	0.777	6.61×10^{-14}	22,200	8.91×10^{-18}	17,900	0.472
Montmor-Na[7]	1.66×10^{-10}	0.337	1.95×10^{-13}	48,000	0.22	3.89×10^{-15}	48,000	3.90×10^{-12}	78,000	-0.13
Albite[3]	2.75×10^{-9}	0.010	0.7	58,000	0.3	2.05×10^{-1}	60,000	1.50×10^{-5}	50,000	-0.35
Hematite[4]	2.51×10^{-15}	0.011	2.57×10^{-9}	66,200	1	2.52×10^{-15}	66,200	–	–	–
Pyrite[2]	2.82×10^{-5}	0.011	3.02×10^{-8}	50,800	-0.5	2.00×10^{-10}	50,800	2.82×10^{-5}	56,900	0.5
TU-2										
Quartz[3]	2.00×10^{-14}	0.022	4.03×10^{-4}	45,600	0.309	–	–	0.105	80,000	-0.41
Muscovite[3]	4.40×10^{-12}	0.014	1.26×10^{-4}	41,311	0.37	6.31×10^{-6}	39,301	3.16×10^{-5}	56,950	-0.22
Montmor-Na[7]	1.66×10^{-12}	0.119	1.95×10^{-13}	48,000	0.22	3.89×10^{-15}	48,000	3.90×10^{-12}	78,000	-0.13
Montmor-Ca[7]	1.66×10^{-14}	0.119	1.95×10^{-13}	48,000	0.22	3.89×10^{-15}	48,000	3.90×10^{-12}	78,000	-0.13
Albite[3]	2.75×10^{-9}	0.010	0.7	58,000	0.3	2.05×10^{-1}	60,000	1.50×10^{-5}	50,000	-0.35
Andalusite[9]	3.00×10^{-7}	0.019	–	–	–	3.83	73,500	–	–	–
Hematite[4]	2.51×10^{-16}	0.011	2.57×10^{-9}	66,200	1	2.52×10^{-15}	66,200	–	–	–
Pyrite[2]	2.82×10^{-5}	0.011	3.02×10^{-8}	50,800	-0.5	2.00×10^{-10}	50,800	2.82×10^{-5}	56,900	0.5
TU-3										
Quartz[3]	2.00×10^{-14}	0.014	4.03×10^{-4}	45,600	0.309	–	–	0.105	80,000	-0.41
Muscovite[3]	4.40×10^{-12}	0.013	1.26×10^{-4}	41,311	0.37	6.31×10^{-6}	39,301	3.16×10^{-5}	56,950	-0.22
Paragonite[2]	2.51×10^{-14}	0.013	–	–	–	7.15×10^{-10}	22,000	–	–	–
Andalusite[9]	3.00×10^{-7}	0.020	–	–	–	3.83	73,500	–	–	–
Hematite[4]	2.51×10^{-16}	0.011	2.57×10^{-9}	66,200	1	2.52×10^{-15}	66,200	–	–	–
Pyrite[2]	2.82×10^{-5}	0.011	3.02×10^{-8}	50,800	-0.5	2.00×10^{-10}	50,800	2.82×10^{-5}	56,900	0.5
Brucite[2]	3.02×10^{-10}	0.268	4.00×10^{5}	59,000	0.5	1.30×10^{-1}	42,000	-	–	–

[2] From (Palandri and Kharaka, 2004)

[3] From Carbfix_kin.dat database (Heřmanská et al., 2022)

[4] From (Heřmanská et al., 2020)

[7] Based on Montmorillonite (K0.318(Si3.975Al0.025)(Al1.509Fe0.205Mg0.283)(OH)2) from Palandri and Kharaka (2004)

[8] From (Smith et al., 2017)

[9] Based on Kyanite from Marty et al. (2015)

of nonideal mineral crystallinity (Heřmanská et al., 2022; Palandri and Kharaka, 2004). Most of these data have not yet been established, which often hinders accurate modeling of the temporal evolution of natural water-rock systems. While compiling a consistent mineral dissolution database, Heřmanská et al. (2022) found that a typical difference between computed and measured rates is *ca* 0.5 log units. Furthermore, multi-oxide minerals may not dissolve stoichiometrically but more complexly with distinct metal-oxygen bonds breaking at different rates (Heřmanská et al., 2022; Oelkers and Gislason, 2001a).

Another rate-controlling factor is the reactive mineral surface area, which can be measured by inert gas adsorption techniques (BET) or estimated by assuming all particles have an equally sized geometric shape. Using the geometric surface area is common because BET measurements are mostly conducted on whole rock samples, not separated minerals. In this study, we had the advantage of comparing the model results with our experimental observations. The model's mineral surface areas could be adjusted to reach fitting results. We found that the calculated geometric surface areas adequately fit the experimental data. An additional difficulty arises from the incapacity of the model to properly deal with solid solutions. Most of the analyzed mineral phases here have nonideal compositions, and this is not considered during the model calculations, which inevitably results in discrepancies between model and experimental observations. Considering these limitations, our modeling results are discussed in the sections below.

4.2. Basaltic rock

The observed *in-situ* precipitates match common alteration products encountered in the Hengill volcanic system in Iceland (Snæbjörnsdóttir et al., 2018b). Anhydrite, however, is not typically reported from that area but is known from Ocean Drilling Program cores and active hydrothermal seafloor alteration. At these sites, Ca-enriched hydrothermal fluids mix with SO_4-enriched seawater at temperatures above 150 °C (Chen et al., 2013). The high SO_4 content of the initial experimental solution (Table 3) and the Ca supply from basalt dissolution facilitated anhydrite formation during the experiment discussed here.

The initial fluid composition was enriched in SO_4 and Si but contained only low concentrations of Al, Ca, Mg, or Fe (Table 3). Fast dissolution reactions with basaltic rock powder initially supplied these cations at the onset of the experiment. This process initiated silicate and anhydrite precipitation and decreased Si, Al, Na, and K concentrations in the solution (Fig. 6). In contrast, Ca remained at a relatively constant and low concentration level, indicating that the supply of Ca from basaltic rock dissolution probably limited the formation of anhydrite and zeolite. Although precipitation was the dominating reaction process before CO_2 injection, the demand for Ca required simultaneous basalt dissolution. Hence, other cations, such as Mg and Fe, were also released. Like Ca, the Mg and Fe concentrations changed only within limited boundary conditions, indicating that chlorites and clays precipitated as soon as Mg and Fe became available. The decrease in Na is attributed to the formation of Na-Ca-zeolites on the sample and the reactor wall. Wairakite has been shown to develop substantial solid solutions towards analcime in quartz-free environments at high temperatures (Liou et al., 1991), which aligns with the high Na content of the wairakite formed here.

The injection of the CO_2-rich fluid had three main effects on the
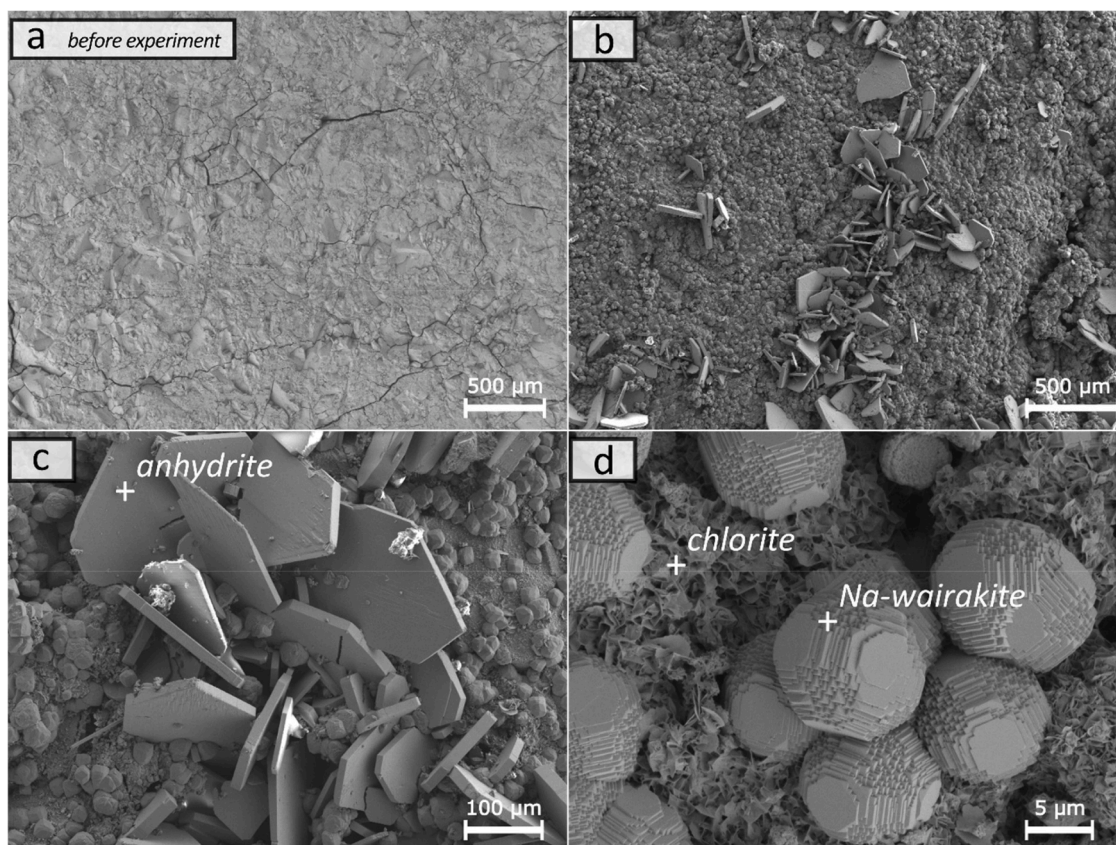
Fig. 4. SEM images of the Icelandic basalt before (a) and after (b-d) the experiment IC-1. After the experiment, chlorite, anhydrite, and Na-wairakite crystals covered the formerly barren sample surface.

Table 6

Compositions of newly formed minerals measured by XRD and EDX on the altered sample material after the experiments. Note that only elements heavier than carbon could be detected by EDX analysis. The accuracy of EDX analyses may have suffered from interferences between mineral phases, resulting in mixed signals.

Secondary minerals			
Sample	Mineral	XRD	EDX
IC-1	Wairakite-analcime-solid solution	$(Ca_{7.52}Na_{1.12})(Al_{15.73}Si_{32.27}O_{96})...(H_2O)_{16}$	$Ca_{0.08}Na_{0.14}Al_{0.55}Si_{1.00}O_{2.62}$
	Chamosite	$(Fe,Al,Mg)_6(Si,Al)_4O_{10}(OH)_8$	$Fe_{0.84}Mg_{0.23}Al_{0.67}Si_{1.00}O_{3.72}Ti_{0.07}Ca_{0.06}S_{0.01}$
	Anhydrite	$CaSO_4$	$Ca_{0.44}S_{1.00}O_{3.37}$
	Clay	–	$Fe_{0.18}Ca_{0.14}Na_{0.09}Mg_{0.07}Ti_{0.02}K_{0.01}Al_{0.64}Si_{1.00}O_{3.24}$
	Diopside	$CaMg_{0.52}Fe_{0.48}(Si_2O_6)$	–
	Ferrosilite	$FeSiO_3$	–
	Aerinite	$((Fe^{2+},Fe^{3+},Al)_3Mg_3(Ca,Na)_4$ $...(Si_{13.5}Al_{4.5}O_{42})(OH)_6)...11\cdot3H_2O$	–
	Precipitation on reactor wall:		
	Analcime	–	$Na_{0.26}Al_{0.25}Si_{1.00}O_{2.79}$
	Clinoptilolite-Na	–	$Na_{0.12}K_{0.03}Al_{0.17}Si_{1.00}O_{2.31}$
TU-1	Nontronite	–	$Fe_{0.54}Na_{0.17}Mg_{0.07}K_{0.06}Al_{0.44}Si_{1.00}O_{4.41}$
	Precipitation on reactor wall:		
	Si-oxide	–	$Si_{1.00}O_{1.26}$
TU-2	Precipitation on reactor wall:		
	Kogarkoite	–	$Na_{3.71}F_{1.35}K_{0.02}Si_{0.04}S_{1.00}O_{4.93}$
	Na-oxide	–	$Na_{1.00}O_{0.51}$
	Na-sulfate	–	$Na_{3.54}S_{1.00}O_{4.77}$
TU-3	Precipitation on reactor wall:		
	Si-oxide	–	$Si_{1.00}O_{2.03}Na_{0.02}Al_{0.01}$

system. First, as distilled water was injected, the element concentrations became diluted. Secondly, the fluid volume in the reactor increased to approximately the initial volume before the extraction of the first samples. Due to that process, precipitates at the reactor wall (the former water table) are inundated again. Thirdly, the dissolved CO_2 lowers the pH to an unknown extent because measurements had to be conducted

after sample extraction in conjunction with decompression and degassing. After CO_2 injection, the rising pH and Si, Al, Na, and K concentrations indicate that the system changed from precipitation-dominated to dissolution-dominated. The CO_2 concentration in the solution could not be monitored with the experimental setup, and it is unclear whether the calcite in the altered sample powder is of primary or
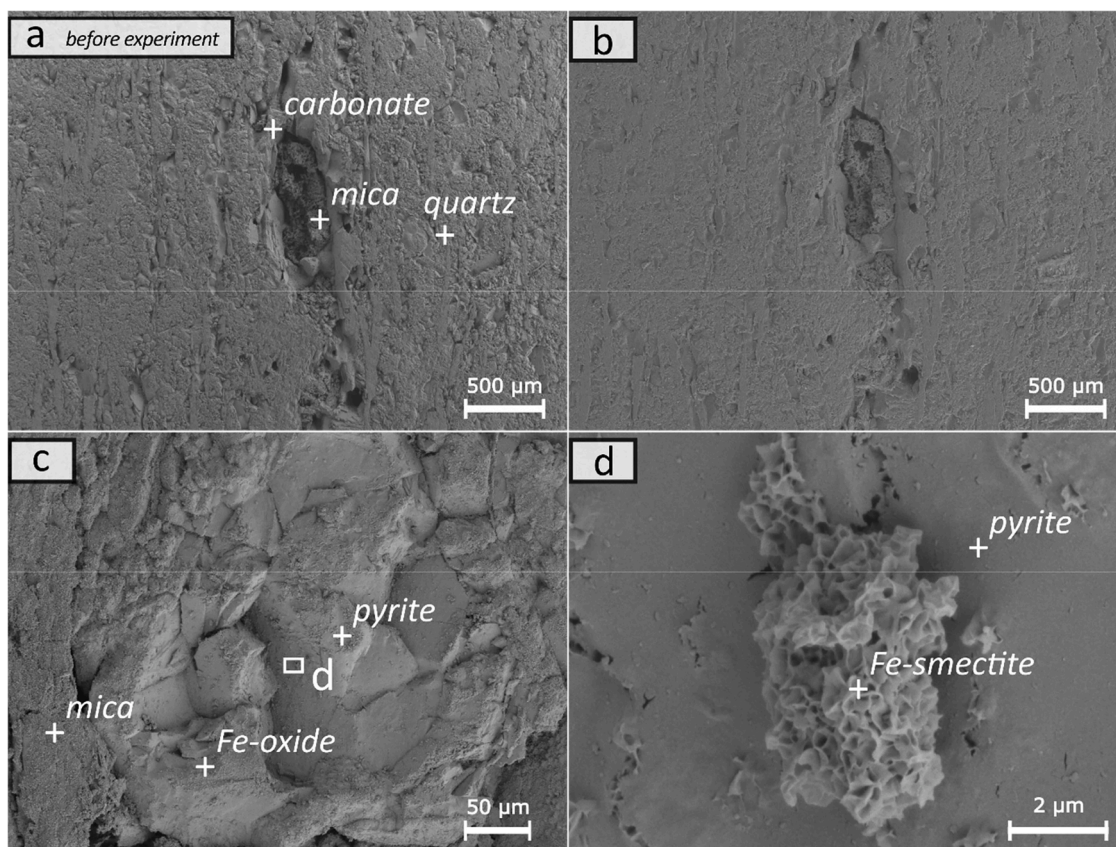
Fig. 5. SEM images of the Turkish metasedimentary rock sample TU-1 before (a) and after (b-d) the experiment. Image d is a magnified section of image c. Apart from small aggregates of Fe-rich smectite (image d), no mineral precipitations were observed on the sample surface after the experiment.

secondary origin. Carbonate minerals, therefore, might have formed during the experiment but were not detected on the analyzed sample surface.

The apparent lack of carbonate precipitation comes as a surprise given that previous studies have either successfully mineralized CO_2 by reaction with basaltic rocks or predicted sequestration with model simulations (Aradóttir et al., 2012; Galeczka et al., 2022; Gysi, 2017; Gysi and Stefánsson, 2008, 2011, 2012a, 2012b). It is relevant that most of these experiments and simulations were conducted at temperatures lower than 100 °C. Interestingly, Gysi and Stefánsson (2012b) conducted experiments at temperatures of up to 250 °C, close to the adopted upper-temperature limit for CO_2 sequestration of Ca 280 °C (Clark et al., 2020). These authors found that sequestration of CO_2 is favored at temperatures of Ca 75 °C. Around this temperature, Ca, Mg, and Fe are mainly incorporated into carbonates, whereas at significantly higher temperatures, clays and zeolites dominate the uptake of divalent cations. This outcome agrees with the observations presented here, except that Gysi and Stefánsson (2012b) reported at least some calcite formation from their high-temperature experiment. In the author's view, the absence of neoformed calcite in the present study is probably attributed to the initial fluid composition. The initial fluid was considerably enriched in most elements compared to the natural spring water from Vellankatla (Table 3) used in the study by Gysi and Stefánsson (2012b). Particularly, the high Si and SO_4 concentrations in the effluent water from well NJ-18 discriminated the preferential incorporation of Ca into zeolite and anhydrite over calcite. Carbonate precipitation might be achieved with a more dilute fluid composition, where silicon becomes a limiting factor instead of Ca. Another factor that promotes the formation of silicates over carbonates might be the presence of O_2. However, since the solutions were treated with nitrogen before the experimental start, free oxygen was expected to be removed.

Marieni et al. (2021a) modeled the reaction path with basalt and either CO_2-charged fresh- or saltwater at various temperatures. As expected, they found that water composition significantly affects the system's mineralogy and chemistry of neoformed minerals. Their freshwater model at 260 °C produced no anhydrite but incorporated Ca preferentially into calcite. The fluid from well NJ-18 is similar in composition to the freshwater of Marieni et al. (2021a) (Table 3) but yields twice as much SO_4. Nevertheless, we observed anhydrite but no calcite in the secondary mineral assemblage, an observation that the higher SO_4 content might best explain. Marieni et al. (2021a) did not include zeolites in their 260 °C models as they did not consider zeolites stable at temperatures above 200 °C. The experiments presented here demonstrated that Ca-Na-zeolites form at 260 °C and compete with anhydrite and calcite for Ca cations. These findings confirm that *in-situ* CO_2 sequestration is limited at high temperatures when the solution chemistry allows silicate precipitation.

4.2.1. Kinetic batch reaction model - Basalt

Despite the above-described limitations, we included kinetic data in our geochemical model to allow a better comparison to the measured temporal fluid evolution. By doing so, we aimed to reproduce geochemical data from a complex multiphase system with currently available kinetic mineral parameters.

The kinetic batch reaction model produced a fluid evolution that mostly conforms with the experimental results (Fig. 6). Discrepancies are mainly visible during the equilibration phase before CO_2 injection. Fast and non-steady state dissolution at the beginning of the experiment caused a rapid enrichment in K, Na, and Al. This feature is likely attributed to the preferential removal of alkali and alkaline earth metals from the basaltic glass structure and damaged crystal lattices of crushed minerals (Heřmanská et al., 2022; Oelkers and Gislason, 2001a). The
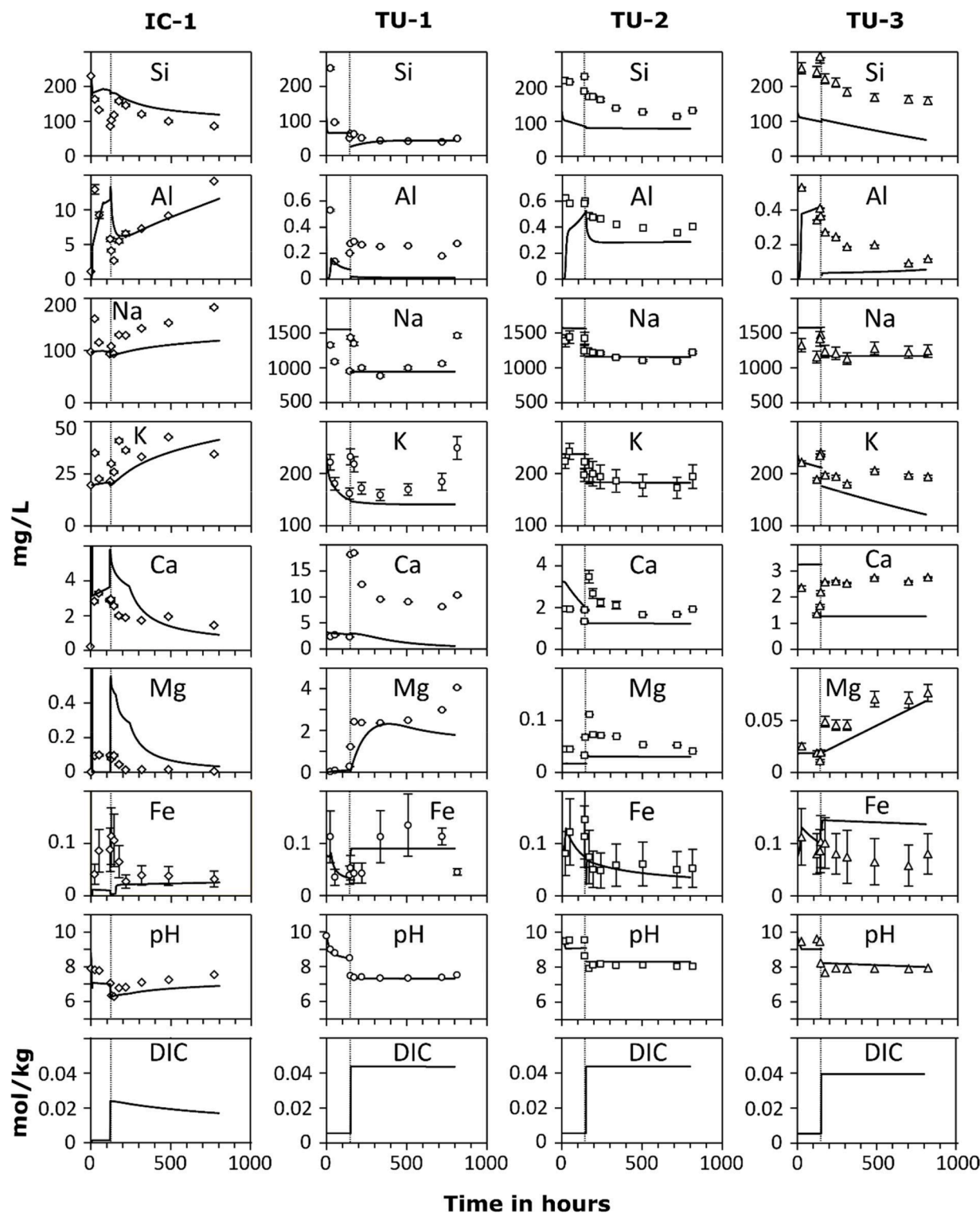
Fig. 6. Evolution of the fluid chemistry during the Icelandic basalt (IC-1) and Turkish metasedimentary rock (TU-1, TU-2, TU-3) experiments. The data points represent the measured compositions. The solid lines show the results of the PHREEQC modeling, and the vertical dotted line indicates the time of CO_2 injection. Error bars are included for all measurements but do not always exceed the size of symbols.

model applied here does not consider this effect. After the initial enrichment, Na and Al concentrations decreased together with Si, a feature that results from Na-Ca-zeolite precipitation. The model does not predict zeolite precipitation before CO_2 is injected because Ca is consumed by anhydrite and diopside (Fig. 7). After adding CO_2, anhydrite and diopside are modeled to dissolve, allowing zeolites to form.

In contrast, the experiment has shown that anhydrite and zeolite

coexist. Both phases precipitated before CO_2 injection, indicated by the fluid chemistry, and were confirmed by a second experiment, which lasted only 120 hours without injection of CO_2. The lack of zeolite precipitation in the model before CO_2 injection explains the opposite trends of the modeled and measured Si and Al concentrations. The model's initial Mg and Ca peaks result from abrupt forsterite, anorthite, and calcite dissolution. The released Mg and Ca are immediately
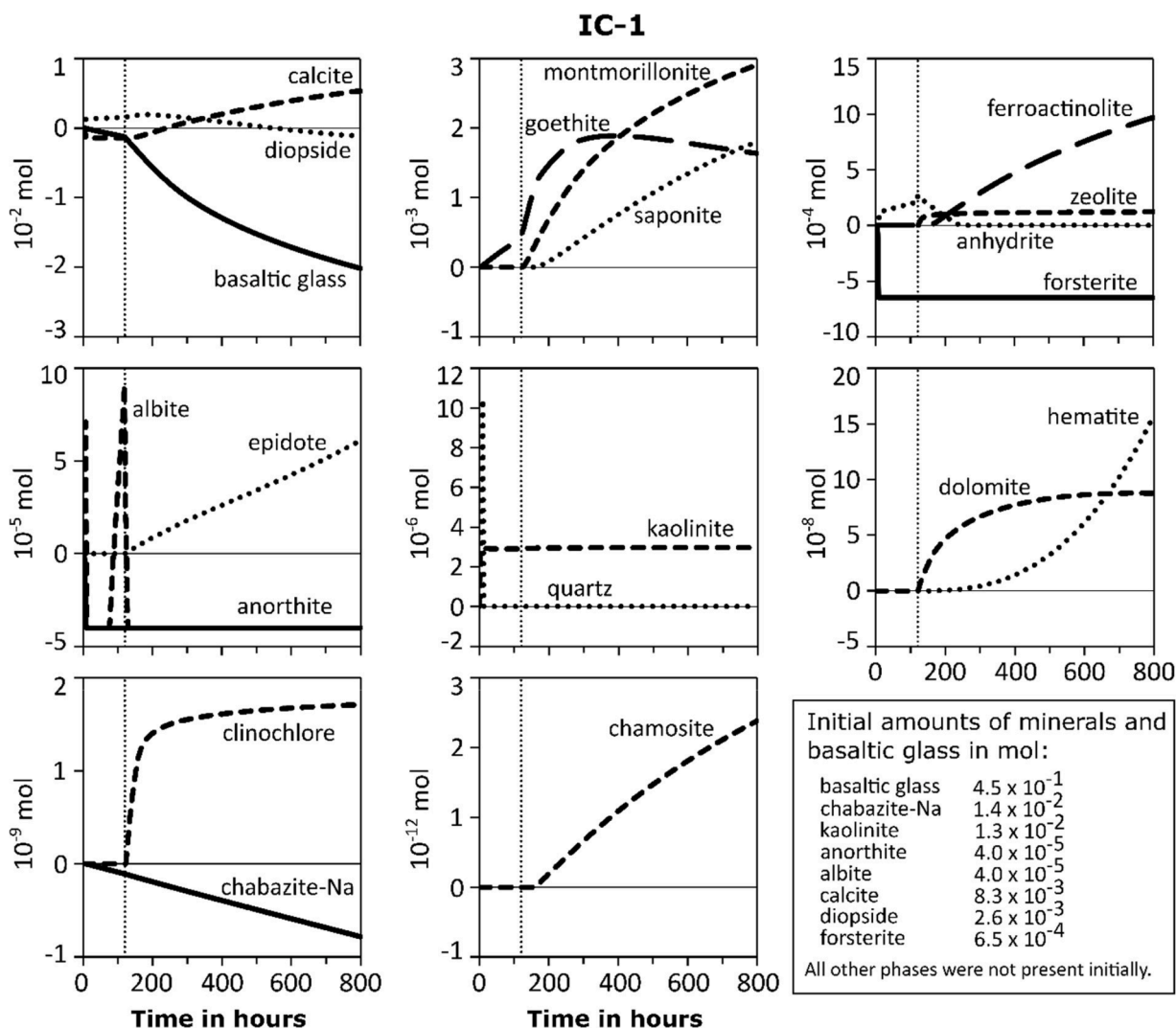
Fig. 7. Results of the PHREEQC modeling of experiment IC-1. Shown is the deviation of mineral phases from their initial amount at the beginning of the experiment. Negative values indicate dissolution, and positive values indicate precipitation. The vertical dotted line indicates the time of CO_2 injection. Montmorillonite represents the sum of a group of minerals, including the montmorillonite K-, Mg-, and Na-varieties. Saponite represents the sum of a group of minerals, including the saponite Fe-Fe-, Fe-K-, Mg-Mg-, Mg-K-, and Mg-Fe-varieties.

incorporated into diopside, anhydrite, and clay minerals. Chlorite was identified as the main Fe sink in the secondary mineral assemblage of the experiment. In the model, goethite is the first phase consuming Fe, while Fe-rich chlorite and clays form only after CO_2 injection. After CO_2 injection, basalt dissolution becomes the dominant process. The constant low concentrations of Ca, Mg, and Fe indicate that the supply of these elements is a limiting factor for the precipitation of zeolite, clay, chlorite, and ferro-actinolite. The incorporation of Mg and Fe into clay minerals at temperatures of about 250 °C was also inferred from monitoring well data during the CarbFix2 CO_2 and H_2S injection campaign at the Hellisheidi geothermal field (Clark et al., 2020).

Furthermore, the model calculation predicts the precipitation of hematite, epidote, dolomite, and calcite. Approximately one-third of the added 22.5 mmol/l CO_2 was modeled to be sequestered mainly into calcite and minor dolomite after 30 days of reaction. This indicates the potential for carbon sequestration in basaltic rocks even at high temperatures, although our experimental results did not produce clear evidence for newly formed carbonates.

Most newly formed zeolites represent a solid solution between wairakite and analcime, but the model calculations do not adequately consider such solid solutions. Thus, Ca can be incorporated into calcite as the model does not form zeolites in large quantities. The PHREEQC

calculation is based on the law of mass action, which has limitations when applied to complex geochemical systems. Alternatively, the Gibbs energy minimization method can overcome some limitations (Gysi, 2017; Leal et al., 2017). Regarding solid solutions, the Gibbs Energy minimization method considers the thermodynamic properties of the solid solution system, such as the temperature and pressure, as well as the chemical potentials of the individual components in the solution. This allows for a more accurate prediction of the concentration of each component in the solid solution, as well as the direction of any phase transitions that may occur.

On the other hand, the law of mass action only considers the reaction equilibrium constant, which does not account for the thermodynamic properties of the system and would not be as accurate in predicting the behavior of the solid solution. However, using the Gibbs Energy minimization approach, the thermodynamic databases are unavailable for metamorphic and basaltic hydrothermal systems in software packages such as GEMS (Kulik et al., 2012). Despite these limitations, the applied model could reproduce the experimental observations with comprehensible discrepancies.

Previous studies have already pointed out that there is an upper-temperature limit for CO_2 sequestration of *ca* 280 °C and that at temperatures above 180 °C silicate minerals compete with carbonate

minerals for the uptake of divalent cations (Clark et al., 2020; Galeczka et al., 2022). Nonetheless, model calculations for the high-temperature CO_2 storage projects at Hellisheidi and Nesjavellir predicted that large quantities of CO_2 would become mineralized, similar to our model results. However, in contrast to previous studies, we combined our model with experimental work, which showed that model calculations might overestimate the CO_2 mineralization efficiency close to the upper-temperature limit for CO_2 sequestration. Our results have shown that this is mainly due to silicate mineral reactions not considered by these models (e.g., the formation of zeolite solid solutions).

4.3. Metasedimentary rocks

Following the experiment with sample TU-1, small aggregates of Fe-rich smectite formed near pyrite and Fe-oxide minerals (Fig. 5). Other precipitates were not detected on the sample surface, but Si-oxide was found on the reactor walls. Smectite formation aligns with field observations from Kızıldere, where smectites are associated with the hydrothermal alteration of carbonate-rich rocks (Bozkaya et al., 2018). XRD analysis of the altered sample powder did not reveal significant mineralogical changes during the experiment, except for gypsum. Gypsum was detected in the fresh but not in the altered sample. This either demonstrates that gypsum was dissolved during the experiment or that gypsum is not distributed homogeneously in the sample and was absent in the analyzed powder fraction. Gypsum was also not observed in the context of SEM or thin-section microscopy. The decreasing pH at the experiment's beginning indicates that precipitation occurs, particularly Si-oxide formed at the reactor walls. Injection of the CO_2-rich fluid caused an increase in the concentrations of Ca and Mg, attributed to carbonate dissolution (Fig. 6).

Experiments TU-2 and TU-3 produced less variable fluid compositions and no secondary minerals apart from the reactor wall scaling. Hence, deducing the mineral reactions was more difficult. The kinetic batch reaction model was used to gain more insight into this process.

In summary, there are no indications of CO_2 sequestration from the three experiments using metasedimentary rocks. These rocks may not be suitable for CO_2 mineralization as the minerals building these rocks provide an insufficient supply of divalent cations. Nearly all of the Ca and Mg present is bound to carbonates, and the small amount of Fe released from pyrite alteration is directly incorporated into clay minerals. Concluding, the experimental observations suggest that the mineralogical composition of the tested metasediments prevents effective CO_2 mineralization.

4.3.1. Kinetic batch reaction model - Metasediments

The metasedimentary rock models did not produce an adequate match with the experimental results when applying the literature kinetic rate data. The rates shown in the literature were determined for dissolution reactions in pure mineral systems, and our modeling efforts have shown that these data are not conferrable to multi-mineral systems without limitations. Potential reasons for this are discussed in Section 4.2. In contrast, kinetic rate data from the literature reasonably agree with the basaltic rock experiment presented here. The basaltic sample consists mainly of basaltic glass, the predominant dissolving phase with a well-described kinetic dissolution rate expression (Gislason and Oelkers, 2003; Oelkers and Gislason, 2001b).

On the other hand, the metasedimentary rocks consist mainly of quartz that does not take part in the dissolution reactions. Clay minerals and andalusite, which only form a minor part of the sample mineralogy, are the main dissolving phases here. The clay minerals and solid mica solutions are complex and heterogeneous in composition, rendering applying general kinetic rate data for these mineral groups problematic. Through matching with the experimental data, we derived new rate constants that describe our particular rock-fluid system more accurately.

In model TU-1, muscovite, albite, and dolomite form at the expense of illite and kaolinite. In model TU-2, muscovite and albite are forming

at the expense of andalusite, and in model TU-3, muscovite forms from andalusite and brucite dissolution (Fig. 8). Moreover, in all three models, hematite forms from pyrite alteration. We did not observe neoformed muscovite minerals on the sample surfaces, but muscovite might have formed in the pore space of the sample powder. Besides, EDX analysis revealed that the composition of micas was partially altered during the experiments towards higher relative O, Na, and Fe contents. This indicates that micas were altered complexly by forming solid solutions that could not be accurately modeled. The low Al concentrations, especially in the models after CO_2 injection, indicate that Al is a limiting factor for mica precipitation. In models TU-2 and TU-3, mica precipitation depends on Al release from andalusite dissolution. The modeled Na concentrations are relatively invariable compared to the measured fluid. What reactions might have controlled the Na variation in the measured solution remains unclear, as no mineral phase contains significant amounts of Na. Albite was considered a potential control on Na in the models, but no albite was detected on the sample surface after the experiment. Albite might, however, have formed but remained undetected in the sample powder.

Ca and Mg are consumed by dolomite in model TU-1. While Mg is supplied from illite dissolution, there is no effective source for Ca. Thus, Ca is a limiting factor for dolomite formation in model TU-1. Compared to the experimental data, the Ca response to CO_2 injection is much lower in model TU-1. This discrepancy might result from small amounts of calcite dissolved after CO_2 injection, but calcite was absent in the model. For sample TU-3, the experimental results indicate an increase of Mg in the solution, which was addressed by adding a small amount of brucite to dissolve in the model.

While the experiments using metasedimentary rocks did not show any indications for carbon sequestration, the results of model TU-1 do predict the formation of dolomite when sufficient Mg is supplied. In the llnl.dat database, illite contains Mg and represents the Mg source in the model. However, the mineralogical analysis of the metasedimentary rocks has shown that carbonates are the only effective source of Ca and Mg, making carbon sequestration with these elements ineffective. Pyrite alteration forms Fe-oxides and releases only a little Fe into the solution, which is incorporated into smectites rather than carbonates. These findings correlate with the results of 3-D reactive transport modeling by Erol et al. (2022) to analyze mineral reactions during CO_2-fluid injection in the Kızıldere reservoir. These authors also observed the formation of hematite and clays from Fe oxidation at elevated pH. Similar to the results shown here, Erol et al. (2022) conclude that CO_2 does not undergo a significant mineralization process. The model shows that CO_2 mineralization can be achieved with an effective source of Mg or Ca. However, this was not the case for the tested metasediments.

While our results have shown that CO_2 mineralization may not be feasible on a large scale for the Kızıldere geothermal field, the injection of CO_2 is still dependable thanks to solubility-trapping. Reactive transport modeling by Erol et al. (2023) indicates that about 200 kt CO_2 can be injected safely into the reservoir for ten years. The power plant's emissions can still be reduced to some extent.

5. Conclusion

The batch reaction experiments with one basaltic and three metasedimentary rock samples produced valuable insight into rock-fluid-CO_2 interaction processes from which potentials and challenges for *in-situ* CO_2 mineralization can be deduced.

The experimental and modeling results indicate that the mineralogy of glassy basaltic rocks is suitable for a sufficient supply of divalent cations necessary for CO_2 sequestration. However, according to the results from the batch reactor experiment, the high temperature of 260 °C favors incorporating these cations into zeolite, chlorite, and anhydrite rather than carbonate. In contrast, the PHREEQC simulation of the experiment predicts calcite formation. Although it cannot be excluded that carbonates might have formed undetected during the experiment,
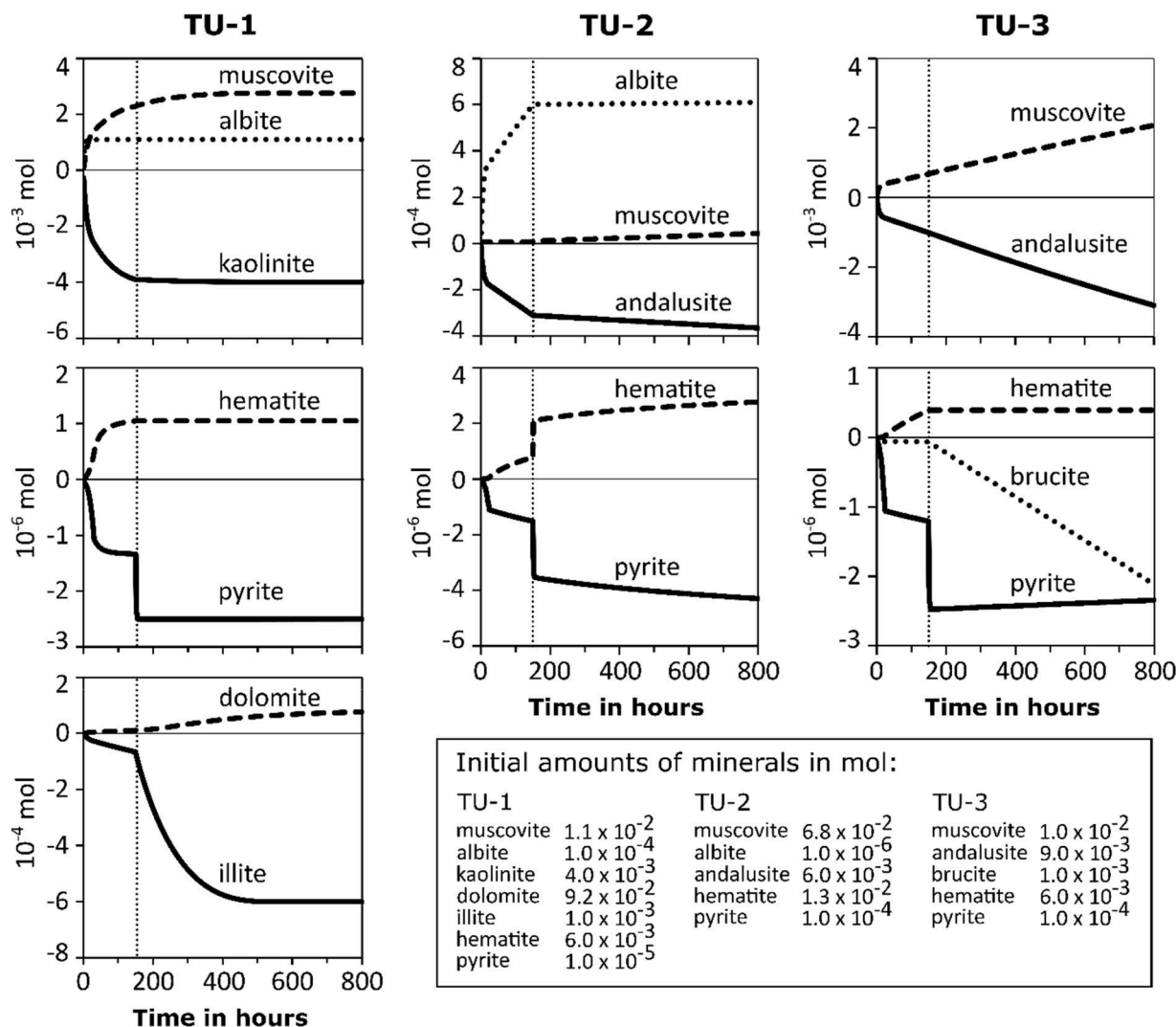
Fig. 8. Results of the PHREEQC modeling of experiments TU-1, TU-2, and TU-3. The deviation of mineral phases from their initial amount at the beginning of the experiment is shown. Negative values indicate dissolution, and positive values indicate precipitation. The vertical dotted line indicates the time of CO_2 injection.

this discrepancy most probably results from the inability of the model to deal properly with solid solutions. Solid solutions between wairakite and analcime were identified as the main secondary Ca phase in the experiment. The model did not consider such solid solutions, so Ca was incorporated into calcite.

This study illustrates that numerical modeling alone can be misleading and is best combined with experimental work to validate the results. While previous models (Galeczka et al., 2022; Marieni et al., 2021a) and the experiments of Gysi and Stefánsson (2012b) documented the potential for CO_2 sequestration even at high temperatures, our results emphasize the importance of suitable geochemical boundary conditions. In our case, the geochemical model predicted CO_2 mineralization, although the experiment showed silicate instead of carbonate formation. This leads to a modeled overestimation of the CO_2 sequestration potential and illustrates that geochemical model calculations must be treated carefully.

For the experiments using metasedimentary rocks, a lower temperature of 105 °C was applied, representing the downhole temperatures of the Kızıldere reservoir. Even though lower temperatures are reportedly better suited for the CO_2 mineralization process, large-scale CO_2 sequestration cannot be expected because the metasedimentary rocks' mineralogy cannot supply the required divalent cations. Calcium and Mg are, for the most part, already bound to carbonates, and the small amounts of iron released from pyrite alteration are preferentially

incorporated into clay minerals. For the CO_2 storage project at the Kızıldere geothermal reservoir, the results of this study imply that mineralization is not a feasible storage mechanism. It would be advised to focus on an alternative mechanism like solubility trapping.

Modeling the results of the experiments using metasedimentary rocks was challenging because the literature on mineral kinetic rate constants could not reproduce the kinetic reactions of such complex multiphase systems. Therefore, by matching the results from the batch reactor experiments, we estimated new kinetic rate constants that apply specifically and exclusively to the systems considered here. With these calculated rate constants, we could adequately reproduce the experimental results. However, discrepancies between the models and experimental observations remain because the program cannot properly deal with solid solutions, making modeling complex nonideal phases difficult. This problem may be resolved using the Gibbs energy minimization methods instead of the law of mass action for future modeling calculations (Kulik, 2006; Kulik et al., 2012; Thien et al., 2014).

Regarding the basaltic rock, it would be beneficial to repeat the experiment with a longer run time and more dilute fluid composition to test whether the initial enrichment in Si and SO_4 has facilitated silicate and sulfate precipitation instead of carbonate. Modeling the reactions with the metasedimentary rocks has shown that CO_2 sequestration may be feasible if a Mg- or Ca-supplying phase is present, and the results encourage extending this research to rock types other than basalt.

However, the authors believe mineralogies with a more suitable composition should be applied compared to the metasediments tested here.

CRediT authorship contribution statement

Maximilian Berndsen: Conceptualization, Methodology, Software, Validation, Investigation, Writing – original draft, Writing – review & editing, Visualization. **Selçuk Erol:** Conceptualization, Methodology, Software, Validation, Investigation, Writing – original draft, Writing – review & editing, Project administration. **Taylan Akın:** Conceptualization, Methodology, Software, Project administration. **Serhat Akın:** Supervision. **Isabella Nardini:** Conceptualization, Supervision, Project administration. **Adrian Immenhauser:** Supervision, Writing – review & editing. **Mathias Nehler:** Conceptualization, Methodology, Investigation, Supervision.

Declaration of Competing Interest

The authors declare that they have no known competing financial interests or personal relationships that could have appeared to influence the work reported in this paper.

Acknowledgments

References

Aradóttir, E., Sonnenthal, E.L., Björnsson, G., Jónsson, H., 2012. Multidimensional reactive transport modeling of CO_2 mineral sequestration in basalts at the Hellisheidi geothermal field, Iceland. Int. J. Greenhouse Gas Control 9, 24–40. https://doi.org/10.1016/j.ijggc.2012.02.006.

Blasco, M., Gimeno, M.J., Auqué, L.F., 2017. Comparison of different thermodynamic databases used in a geothermometrical modelling calculation. Procedia Earth Planet. Sci. 17, 120–123. https://doi.org/10.1016/j.proeps.2016.12.023.

Bozkaya, Ö., Bozkaya, G., Ganiz, İ., Akın, T., Kaya, A., 2018. Kızıldere Jeotermal Sahası Hidrotermal Alterasyon Zonlarının. Mineralojisi ve Sıvı Kapanım Verileri. 4th Geothermal Resources and Natural Mineral Waters Symposium and Exhibition. Afyonkarahisar, Turkey.

Brunauer, S., Emmett, P.H., Teller, E., 1938. Adsorption of gases in multimolecular layers. J. Am. Chem. Soc. 60 (2), 309–319. https://doi.org/10.1021/ja01269a023.

Chen, S., Wang, X., Yin, X., Zhang, G., 2013. Genesis of anhydrite in hydrothermally altered basalt from the East Pacific Rise near 13°N. Acta Oceanol. Sin. 32 (2), 12–17. https://doi.org/10.1007/s13131-013-0270-z.

Clark, D.E., Gunnarsson, I., Aradóttir, E.S., Þ. Arnason, M., Þorgeirsson, Þ.A., Sigurðardóttir, S.S., Sigfússon, B., Snæbjörnsdóttir, S.Ó., Oelkers, E.H., Gíslason, S. R., 2018. The chemistry and potential reactivity of the CO_2-H_2S charged injected waters at the basaltic CarbFix2 site, Iceland. Energy Procedia 146, 121–128. https://doi.org/10.1016/j.egypro.2018.07.016.

Clark, D.E., Oelkers, E.H., Gunnarsson, I., Sigfússon, B., Snæbjörnsdóttir, S.Ó., Aradóttir, E.S., Gíslason, S.R., 2020. CarbFix2: CO_2 and H_2S mineralization during 3.5 years of continuous injection into basaltic rocks at more than 250°C. Geochim. Cosmochim. Acta 279, 45–66. https://doi.org/10.1016/j.gca.2020.03.039.

Erol, S., Akın, T., Başer, A., Saraçoğlu, Ö., Akın, S., 2022. Fluid-CO_2 injection impact in a geothermal reservoir: Evaluation with 3-D reactive transport modeling. Geothermics 98, 102271. https://doi.org/10.1016/j.geothermics.2021.102271.

Erol, S., AKIN, T., AKIN, S., 2023. Update for reactive transport modeling of the Kızıldere geothermal field to reduce uncertainties in the early inspections. Turkish J. Earth Sci. 32 (4), 541–554. https://doi.org/10.55730/1300-0985.1860.

Franzson, H., 2000. Hydrothermal evolution of the Nesjavellir high-temperature system, Iceland. In: Proceedings of the World Geothermal Congress 2000 Kyushu-Tohoku. Japan, May 28 - June 10, 2000.

Galeczka, I.M., Stefánsson, A., Kleine, B.I., Gunnarsson-Robin, J., Snæbjörnsdóttir, S.Ó., Sigfússon, B., Gunnarsdóttir, S.H., Weisenberger, T.B., Oelkers, E.H., 2022. A pre-injection assessment of CO_2 and H_2S mineralization reactions at the Nesjavellir (Iceland) geothermal storage site. Int. J. Greenhouse Gas Control 115, 103610. https://doi.org/10.1016/j.ijggc.2022.103610.

Gislason, S.R., Oelkers, E.H., 2003. Mechanism, rates, and consequences of basaltic glass dissolution: II. An experimental study of the dissolution rates of basaltic glass as a function of pH and temperature. Geochim. Cosmochim. Acta 67 (20), 3817–3832. https://doi.org/10.1016/S0016-7037(03)00176-5.

Gislason, S.R., Wolff-Boenisch, D., Stefansson, A., Oelkers, E.H., Gunnlaugsson, E., Sigurdardottir, H., Sigfusson, B., Broecker, W.S., Matter, J.M., Stute, M., 2010. Mineral sequestration of carbon dioxide in basalt: a pre-injection overview of the CarbFix project. Int. J. Greenhouse Gas Control 4 (3), 537–545. https://doi.org/10.1016/j.ijggc.2009.11.013.

Gunnarsdóttir, S.H., Akın, S., Weisenberger, T.B., Clark, D.E., Galeczka, I.M., Helgadóttir, H.M., Marteinsson, K., Þorgilsson, G., Akın, T., Baser, A., Erol, S., Kucuk, S., Saraçoğlu, Ö., Trumpy, E., Montegrossi, G., Batini, F., Bonini, M., Brogi, A., Bicocchi, G., Gola, G., Liotta, D., Manzella, A., Montanari, D., Orlando, A., Ronconi, A., Ruggieri, G., Santilano, A., Jagert, F., Nardini, I., Seidel, T., 2021. GECO D2.9: Report on integrated geological and reservoir models and injection modelling.

Gunnarsson, I., Aradóttir, E.S., Oelkers, E.H., Clark, D.E., Arnason, M.Þ., Sigfússon, B., Snæbjörnsdóttir, S.Ó., Matter, J.M., Stute, M., Júlíusson, B.M., Gíslason, S.R., 2018. The rapid and cost-effective capture and subsurface mineral storage of carbon and sulfur at the CarbFix2 site. Int. J. Greenhouse Gas Control 79, 117–126. https://doi.org/10.1016/j.ijggc.2018.08.014.

Gysi, A.P., Stefánsson, A., 2008. Numerical modelling of CO_2 -water-basalt interaction. Mineral. Mag. 72 (1), 55–59. https://doi.org/10.1180/minmag.2008.072.1.55.

Gysi, A.P., Stefánsson, A., 2011. CO_2–water–basalt interaction. Numerical simulation of low temperature CO_2 sequestration into basalts. Geochim. Cosmochim. Acta 75 (17), 4728–4751. https://doi.org/10.1016/j.gca.2011.05.037.

Gysi, A.P., Stefánsson, A., 2012a. CO2-water–basalt interaction. Low temperature experiments and implications for CO_2 sequestration into basalts. Geochim. Cosmochim. Acta 81, 129–152. https://doi.org/10.1016/j.gca.2011.12.012.

Gysi, A.P., Stefánsson, A., 2012b. Experiments and geochemical modeling of CO_2 sequestration during hydrothermal basalt alteration. Chem. Geol. 306-307, 10–28. https://doi.org/10.1016/j.chemgeo.2012.02.016.

Gysi, A.P., 2017. Numerical simulations of CO_2 sequestration in basaltic rock formations: challenges for optimizing mineral-fluid reactions. Pure Appl. Chem. 89 (5), 581–596. https://doi.org/10.1515/pac-2016-1016.

Heřmanská, M., Marieni, C., Voigt, M., Declercq, J., Oelkers, E.H., 2020. CarbFix Kinetics Database.

Heřmanská, M., Voigt, M.J., Marieni, C., Declercq, J., Oelkers, E.H., 2022. A comprehensive and internally consistent mineral dissolution rate database: Part I: Primary silicate minerals and glasses. Chem. Geol. 597, 120807 https://doi.org/10.1016/j.chemgeo.2022.120807.

Kulik, D.A., Wagner, T., Dmytrieva, S.V., Kosakowski, G., Hingerl, F.F., Chudnenko, K.V., Berner, U.R., 2012. GEM-Selektor geochemical modeling package: revised algorithm and GEMS3K numerical kernel for coupled simulation codes. Comput. Geosci. https://doi.org/10.1007/s10596-012-9310-6.

Kulik, D.A., 2006. Dual-thermodynamic estimation of stoichiometry and stability of solid solution end members in aqueous–solid solution systems. Chem. Geol. 225 (3-4), 189–212. https://doi.org/10.1016/j.chemgeo.2005.08.014.

Langmuir, D., 1997. Aqueous Environmental Geochemistry. Prentice Hall; Prentice-Hall International, Upper Saddle River, NJ, London, 600 pp.

Leal, A.M.M., Kulik, D.A., Smith, W.R., Saar, M.O., 2017. An overview of computational methods for chemical equilibrium and kinetic calculations for geochemical and reactive transport modeling. Pure Appl. Chem. 89 (5), 597–643. https://doi.org/10.1515/pac-2016-1107.

Liou, J.G., Capitani, C.de, Frey, M., 1991. Zeolite equilibria in the system CaAI2Si20₈ - NaAISi₃O₈ - SiO₂ - H₂O. N.Z. J. Geol. Geophys. 34 (3), 293–301. https://doi.org/10.1080/00288306.1991.9514467.

Marieni, C., Voigt, M., Clark, D.E., Gíslason, S.R., Oelkers, E.H., 2021a. Mineralization potential of water-dissolved CO_2 and H_2S injected into basalts as function of temperature: freshwater versus Seawater. Int. J. Greenhouse Gas Control (109). https://doi.org/10.1016/j.ijggc.2021.103357.

Marieni, C., Voigt, M.J., Oelkers, E.H., 2021b. Experimental study of epidote dissolution rates from pH 2 to 11 and temperatures from 25 to 200°C. Geochim. Cosmochim. Acta 294, 70–88. https://doi.org/10.1016/j.gca.2020.11.015.

Marty, N.C., Claret, F., Lassin, A., Tremosa, J., Blanc, P., Madé, B., Giffaut, E., Cochepin, B., Tournassat, C., 2015. A database of dissolution and precipitation rates for clay-rocks minerals. Appl. Geochem. 55, 108–118. https://doi.org/10.1016/j.apgeochem.2014.10.012.

Matter, J.M., Stute, M., Snæbjörnsdottir, S.Ó., Oelkers, E.H., Gislason, S.R., Aradottir, E. S., Sigfusson, B., Gunnarsson, I., Sigurdardottir, H., Gunnlaugsson, E., Axelsson, G., Alfredsson, H.A., Wolff-Boenisch, D., Mesfin, K., La Fernandez de Reguera Taya, D., Hall, J., Dideriksen, K., Broecker, W.S., 2016. Rapid carbon mineralization for permanent disposal of anthropogenic carbon dioxide emissions. Science (New York, N.Y.) 352 (6291), 1312–1314. https://doi.org/10.1126/science.aad8132.

Metz, B., Davidson, O., Coninck, H. de, Loos, M., Meyer, L., 2005. Carbon Dioxide Capture and Storage. Intergovernmental Panel on Climate Change, 443 pp.

Oelkers, E.H., Gislason, S.R., 2001a. The mechanism, rates and consequences of basaltic glass dissolution: I. An experimental study of the dissolution rates of basaltic glass as a function of aqueous Al, Si and oxalic acid concentration at 25°C and pH = 3 and 11. Geochim. Cosmochim. Acta 65 (21), 3671–3681. https://doi.org/10.1016/S0016-7037(01)00664-0.

Oelkers, E.H., Gislason, S.R., 2001b. The mechanism, rates and consequences of basaltic glass dissolution: I. An experimental study of the dissolution rates of basaltic glass as a function of aqueous Al, Si and oxalic acid concentration at 25°C and pH = 3 and 11. Geochim. Cosmochim. Acta 65 (21), 3671–3681. https://doi.org/10.1016/S0016-7037(01)00664-0.

Oelkers, E.H., Schott, J., 2005. Geochemical aspects of CO₂ sequestration. Chem. Geol. 217 (3-4), 183–186. https://doi.org/10.1016/j.chemgeo.2004.12.006.

Oelkers, E.H., Gislason, S.R., Matter, J., 2008. Mineral carbonation of CO₂. Elements 4 (5), 333–337. https://doi.org/10.2113/gselements.4.5.333.

Pabst, A., Sharp, W.N., 1973. Kogarkoite, a new natural phase in the system Na2SO4-NaF-NaC. Am. Mineralog. J. Earth Planet. Mater. 58 (1–2), 116–127.

Palandri, J.L., Kharaka, Y.K., 2004. A compilation of rate parameters of water-mineral interaction kinetics for application to geochemical modeling.

Parkhurst, D.L., Appelo, C.A.J., 2013. Description of Input and Examples For PHREEQC Version 3–A Computer Program For speciation, batch-reaction, One-Dimensional transport, and Inverse Geochemical Calculations. U.S. Geological Survey, p. 497.

Ratouis, T.M., Snæbjörnsdóttir, S.Ó., Sigfússon, B., Gunnarsson, I., Voigt, M.J., Aradottir, E.S., 2021. Reactive transport model of CO₂ and H₂S mineral sequestration at the carbfix2 reinjection site, hellisheidi geothermal power plant, SW-Iceland. In: Proceedings of the World Geothermal Congress 2020+1.

Ratouis, T.M., Snæbjörnsdóttir, S.Ó., Voigt, M.J., Sigfússon, B., Gunnarsson, G., Aradóttir, E.S., Hjörleifsdóttir, V., 2022. Carbfix 2: A transport model of long-term CO₂ and H₂S injection into basaltic rocks at Hellisheidi, SW-Iceland. Int. J. Greenhouse Gas Control 114, 103586. https://doi.org/10.1016/j.ijggc.2022.103586.

Raza, A., Glatz, G., Gholami, R., Mahmoud, M., Alafnan, S., 2022. Carbon mineralization and geological storage of CO₂ in basalt: mechanisms and technical challenges. Earth Sci. Rev. 229, 104036 https://doi.org/10.1016/j.earscirev.2022.104036.

Schott, J., Pokrovsky, O.S., Oelkers, E.H., 2009. The link between mineral dissolution/precipitation kinetics and solution chemistry. Rev. Mineral. Geochem. 70 (1), 207–258. https://doi.org/10.2138/rmg.2009.70.6.

Sigfusson, B., Bragadóttir, R.B., Batini, F., Boschi, C., Freire, L., Gunnarsdóttir, S.H., Halacoglu, U., Ingólfsson, H.P., Manfrida, G., Muller, J., Nardini, I., Oelkers, E.H., Santamaria, A.M., Souque, C., Sposato, F., Stefánsson, A., Snæbjörnsdóttir, S.Ó., Weidmann, D., 2021. GECO - geothermal emission control. In: Proceedings of the World Geothermal Congress 2020+1. Reykjavik, Iceland, April-October 2021.

Smith, M.M., Dai, Z., Carroll, S.A., 2017. Illite dissolution kinetics from 100 to 280°C and pH 3 to 9. Geochim. Cosmochim. Acta 209, 9–23. https://doi.org/10.1016/j.gca.2017.04.005.

Snæbjörnsdóttir, S.Ó., Gislason, S.R., Galeczka, I.M., Oelkers, E.H., 2018. Reaction path modelling of in-situ mineralization of CO₂ at the CarbFix site at Hellisheidi, SW-Iceland. Geochim. Cosmochim. Acta 220, 348–366. https://doi.org/10.1016/j.gca.2017.09.053.

Snæbjörnsdóttir, S.Ó., Sigfússon, B., Marieni, C., Goldberg, D., Gislason, S.R., Oelkers, E. H., 2020. Carbon dioxide storage through mineral carbonation. Nat. Rev. Earth Environ. 1 (2), 90–102. https://doi.org/10.1038/s43017-019-0011-8.

Thien, B.M., Kulik, D.A., Curti, E., 2014. A unified approach to model uptake kinetics of trace elements in complex aqueous–solid solution systems. Appl. Geochem. 41, 135–150. https://doi.org/10.1016/j.apgeochem.2013.12.002.

Voigt, M., Marieni, C., Clark, D.E., Gíslason, S.R., Oelkers, E.H., 2018. Evaluation and refinement of thermodynamic databases for mineral carbonation. Energy Procedia 146, 81–91. https://doi.org/10.1016/j.egypro.2018.07.012.

Wolery, T.J., Daveler, S.A., 1992. EQ6, A Computer Program for Reaction Path Modeling of Aqueous Geochemical Systems: Theoretical Manual, User's Guide, and Related Documentation (Version 7.0). Lawrence Livermore National Laboratory, p. 352.

Žáček, V., Rapprich, V., Šíma, J., Škoda, R., Laufek, F., Legesa, F., 2015. Kogarkoite, Na3 (SO4)F, from the Shalo hot spring, Main Ethiopian Rift: implications for F-enrichment of thermal groundwater related to alkaline silicic volcanic rocks. J. Geosci. 171–179. https://doi.org/10.3190/jgeosci.195.